AFRL-RZ-WP-TR-2009-2064

PROPULSION AND POWER RAPID RESPONSE R&D SUPPORT

Delivery Order 0041: Power Dense Solid Oxide Fuel Cell Systems: High Performance, High Power Density Solid Oxide Fuel Cells− Materials and Load Control

Stephen W. Sofie, Steven R. Shaw, Peter A. Lindahl, and Lee H. Spangler

Montana State University

DECEMBER 2008
Final Report

AIR FORCE RESEARCH LABORATORY
PROPULSION DIRECTORATE
WRIGHT-PATTERSON AIR FORCE BASE, OH 45433-7251
AIR FORCE MATERIEL COMMAND
UNITED STATES AIR FORCE

NOTICE AND SIGNATURE PAGE

AFRL-RZ-WP-TR-2009-2064 HAS BEEN REVIEWED AND IS APPROVED FOR PUBLICATION IN ACCORDANCE WITH ASSIGNED DISTRIBUTION STATEMENT.

*//Signature//	//Signature//
RYAN M. MILLER, Ph.D. Chemical Engineer Thermal & Electrochemical Branch Energy/Power/Thermal Division	THOMAS L REITZ, Ph.D. Branch Chief Thermal & Electrochemical Branch Energy/Power/Thermal Division

*Disseminated copies will show "//Signature//" stamped or typed above the signature blocks.

REPORT DOCUMENTATION PAGE

Form Approved
OMB No. 0704-0188

1. REPORT DATE *(DD-MM-YY)*
December 2008

2. REPORT TYPE
Final

3. DATES COVERED *(From - To)*
19 September 2006 – 26 November 2008

4. TITLE AND SUBTITLE
PROPULSION AND POWER RAPID RESPONSE R&D SUPPORT
Delivery Order 0041: Power Dense Solid Oxide Fuel Cell Systems: High Performance, High Power Density Solid Oxide Fuel Cells−Materials and Load Control

5a. CONTRACT NUMBER
F33615-02-D-2299-0041

5b. GRANT NUMBER

5c. PROGRAM ELEMENT NUMBER
62203F

5d. PROJECT NUMBER
3145

5e. TASK NUMBER
13

5f. WORK UNIT NUMBER
3145130T

6. AUTHOR(S)
Stephen W. Sofie, Steven R. Shaw, Peter A. Lindahl, and Lee H. Spangler

7. PERFORMING ORGANIZATION NAME(S) AND ADDRESS(ES)

By:
Montana State University
P.O. Box 2460
Bozeman, MT 59717-2460

For:
Universal Technology Corporation
1270 N. Fairfield Road
Dayton, OH 45432-2600

8. PERFORMING ORGANIZATION REPORT NUMBER

9. SPONSORING/MONITORING AGENCY NAME(S) AND ADDRESS(ES)
Air Force Research Laboratory
Propulsion Directorate
Wright-Patterson Air Force Base, OH 45433-7251
Air Force Materiel Command
United States Air Force

10. SPONSORING/MONITORING AGENCY ACRONYM(S)
AFRL/RZPS

11. SPONSORING/MONITORING AGENCY REPORT NUMBER(S)
AFRL-RZ-WP-TR-2009-2064

12. DISTRIBUTION/AVAILABILITY STATEMENT
Approved for public release; distribution unlimited.

13. SUPPLEMENTARY NOTES
PAO Case Number: 88ABW 2009-0671, 24 Feb 2009. Report contains color.

14. ABSTRACT

High Performance, High Power Density Solid Oxide Fuel Cells: Materials:

The current geometry and materials set of the state-of-the-art anode supported cell (ASC) yields several deficiencies that limit the performance and robustness of the cell/stack under demanding aero based operational requirements. These deficiencies are embodied in poor gas transport through mechanically strong anodes, the limited use of cerium oxide in the anode due to unfavorable thermal expansion, and the poor thermal stability of ultra fine nickel catalyst under higher temperature operation for maximum output. These deficiencies are being addressed with the development of engineered porous substrates, additives to tailor thermal expansion in ceria based anode systems, and methods for complete infiltration of anode catalysts. Novel ceramic anodes were synthesized and fabricated at Montana State University and characterized through electron microscopy, dilatometry, thermal gravimetry, x-ray diffraction, and electrochemical testing. Modified processing techniques have generated a means for preparing controlled pore morphologies over large areas by freeze casting suitable for anode supported cell fabrication. The use of aluminum titanate additives has demonstrated a 30% decrease in thermal expansion in nickel/ceria anodes and the addition of aluminum titanate to nickel/zirconia porous scaffolds has shown to limit nickel coarsening from high temperature exposure.

Abstract concluded on reverse →

15. SUBJECT TERMS
solid oxide fuel cell, SOFC, solid oxide fuel cell electrodes, SOFC systems, hybrid power systems

16. SECURITY CLASSIFICATION OF:

a. REPORT	b. ABSTRACT	c. THIS PAGE	17. LIMITATION OF ABSTRACT:	18. NUMBER OF PAGES
Unclassified	Unclassified	Unclassified	SAR	54

19a. NAME OF RESPONSIBLE PERSON (Monitor)
Ryan M. Miller

19b. TELEPHONE NUMBER *(Include Area Code)*
N/A

14. ABSTRACT (concluded)

High Performance, High Power Density Solid Oxide Fuel Cells: Load Control:

This report provides a physically-based model for design and optimization of a fuel cell powered electric propulsion system for an unmanned aerial vehicle. Components of the system include a solid oxide fuel cell providing power, motor controller, brushless DC motor, and a propeller. The simulation allows an operator to select constraints and explore design trade-offs between components, including fuel cell, controller, motor, and propeller options. We also present a graphical procedure using this model that allows rapid assessment and selection of design choices, including fuel cell characteristics and hybridization with multiple sources. The simulation model and design techniques are validated using results from a series of tests on an instrumented propulsion system in a low-speed wind tunnel.

TABLE OF CONTENTS

LIST OF FIGURES

LIST OF TABLES

1.0 HIGH PERFORMANCE, HIGH POWER DENSITY SOLID OXIDE FUEL CELLS MATERIALS

1.1 Summary

To achieve the power requirements for implementation of solid oxide fuel cells in unmanned aerial vehicles (UAV), substantial improvements in performance and durability are required to meet the levels required for Air Force implementation. The goal of the proposed research effort is to improve SOFC performance within the confines of the ASC configuration to provide a means of near term implementation, without enacting significant changes to supporting stack architectures. The utilization of engineered pore structures, infiltrated anodes, and low CTE ceria anode technology have been investigated to establish the merits of these research routes and potential performance improvements. The use of freeze casting has demonstrated the ability to tailor pore morphologies conducive to reactant gas delivery and byproduct removal in the generation of continually graded pores with low tortuosity. New casting methods have yielded a degree of long range order not achievable with any other ceramic processing route to date. ASC prototype fabricated with freeze cast anodes achieved greater than 600mW/cm2 at 850°C indicating the strong performance potential of these materials under standard operating conditions. It is expected, however, that these graded porous anodes will show substantial gains under high current operation, which has shown in prior studies to be detrimental to traditional porous anodes. While these anode structures show excellent performance potential, they also demonstrate an inherent lack of mechanical strength in the ASC configuration for which will be phased out in year 2 in favor of more mechanically robust anode architectures. The use of nickel/ceria anodes is limited in ASCs fabrication due to the high coefficient of thermal expansion (CTE) which approaches 14 ppm/°C in contrast to the core electrolyte membranes with a CTE of 10.8 ppm/°C. The addition of aluminum titanate to the anode has yielded the ability to CTE match the anode to the electrolyte with approximately 15wt% dopant. The formation of secondary phases, gadolinium titanate ($Gd_2Ti_2O_7$), may deteriorate anode performance and is a key characterization activity for year two. The use of anode infiltration technologies is designed to mitigate thermal expansion mismatch by using a support constructed of the same material as the electrolyte in the form of a porous/dense bi-layer. The infiltration of the porous component with ultra fine nickel is shown to exhibit rapid thermal degradation due to coarsening of the fine particles. Aluminum titanate was also found to be effective in the infiltration approach by providing chemical anchoring of the nickel catalyst to the underlying scaffold. The electrochemical performance and impedance characterization of the anchored anode approach is another key activity for year two.

1.2 Introduction

1.2.1 Task 1: Microstructurally Engineered Electrodes

High power density fuel cells require increased fuel delivery and byproduct removal. Current state of the art microstructures fabricated with traditional pore forming techniques limit cell current density by the mechanism known as concentration polarization, a condition where fuel demand exceeds the supply. While several fundamental studies aim to determine whether this polarization is a bulk diffusion limitation of hydrogen or water vapor, there is a strong need to optimize interconnected pore morphologies beyond the currently available technologies. Engineered microstructures not only offer decreased tortuosity, thus resulting in cell operation at higher current densities and fuel utilization, but can also offer benefits of cell strength and optimized gas flow characteristics that can yield significant weight losses in stack designs. MSU is developing advanced ceramic processing technologies that allow for microstuctural tailoring of porous SOFC electrodes to achieve graded and aligned pore structures not previously achievable in ceramic materials. These processing techniques are viable for currently used Ni/YSZ and LSM based electrodes and can be used to fabricate traditional anode supported fuel cells, allowing for potentially short term improvements in cell performance and easy integration into current stack technologies.

1.2.2 Task 2: Low CTE Ni/Ceria Anodes

While nickel zironia based anodes have seen immense use given the proven stability, strength, and thermal expansion compatibility, this very common anode is limited by the purely electronic conducting nature of nickel and purely ionic conducting nature of zirconia. This not only limits performance due to discrete triple phase boundary points, but has also shown to be susceptible to both carbonaceous and sulfur bearing fuels. Nickel ceria based anodes have shown dramatically improved performance in pure hydrogen, hydrocarbon, and sulfur laden fuels. While the exact mechanism in which ceria yields benefit are not completely known in all cases, the mixed conducting and catalytic nature of ceria plays an additional role that is not present in the zirconia system. While ceria yields strong benefits, a key downfall is the high thermal expansion coefficient of doped ceria which can exceed 14 ppm/C. Given that most high power fuel cells and stack designs use the anode supported cell configuration, the high CTE of ceria poses thermo-mechanical stress problems that have resulted in excessive cell camber and thermal stress/cycle durability issues. Recently some new custom synthesized low CTE filler compounds have been shown to effectively reduce the CTE of nickel zirconia anodes by approximately 20% with minimal degradation to the performance of the anode. With modification, to address chemical compatibility, the low CTE filler concept may be applied to the nickel ceria anode system to achieve new levels of performance in the standard anode supported package.

1.2.3 Task 3: Solution, Slurry, and Vapor Infiltration of Active Electrodes

This approach focuses on the electrode infiltration of porous zirconia scaffolds utilizing both traditional and engineering pore structures. Electrode infiltration offers the key advantage of low processing temperature 300 – 600°C, thus eliminating deleterious chemical reaction at high temperature allowing a greater selection of more electrochemically active materials. Further, infiltration is not bound by percolation theory which dictates greater than 35% phase content before interconnectivity is achieved, thus allowing the fabrication of anodes with far less metallic content (5 – 20%), allowing for potentially significant weight reductions. A strong benefit not immediately evident is that the thermal expansion of the electrode is dominated by the scaffold, which in this case would be zirconia, allowing excellent CTE matching with electrolyte, reduced cell camber, and greater thermal gradient tolerance for high power/high temperature operation. Additionally, the reduced anode content further allows the use of more exotic materials, even in cost sensitive applications, given the overall reduced volume fraction utilized. Initially, this effort can be focused on anode materials given the complexities with the thick scaffolds and metallic wetting issues, but can be transitioned to cathode as well.

1.3 Experimental Procedure

For Task 1, Nickel oxide powders (Alfa Aesar) and yttrium stabilized zirconia (TZ-8YS, Tosoh) were utilized as received for anode preparation. Aqueous slurries were prepared at 15-35vol% solids loading utilizing an acrylic latex binder system (Duramax B-1001) and ammonium polymethacrylate dispersant (Darvan C). The slurry was poured into an aluminum 8” double doctor blade frame onto a silicone coated Mylar carrier. The carrier was subsequently pulled over a refrigerated aluminum bed (-20 to -40°C) for directional solidification of the tape. The schematic of the freeze tape casting process is shown in Figure 1. The frozen tapes were subsequently treated in a freeze dryer for sublimation of the solvent (water) under a 15 mTorr vacuum. Tapes were cut and sintered at 1400°C for 2hours under ambient conditions and observed by scanning electron microscopy.

For task 2, nickel oxide powders (Alfa Aesar), aluminum titanate (Alfa Aesar), and gadolinium doped ceria (GDC-20, Fuel Cell Materials) were used as received to make anode blends. Anode blend powders were ball milled in aqueous suspension for 24 hours and freeze dryed to achieve homogenous powder batches for uniaxial pressing. Pellets were sintered at 1400°C for two hours. For dilatometry 1cm x 1cm x 2.5cm sample bars were prepared and characterized in both ambient and reducing atmospheres up to 1000°C. Pellets were also characterized by 4-wire DC conductivity to ascertain the reduction in conductivity from the dopant additions. Further, selected pellets were ground mechanically after sintering for x-ray diffraction characterization.

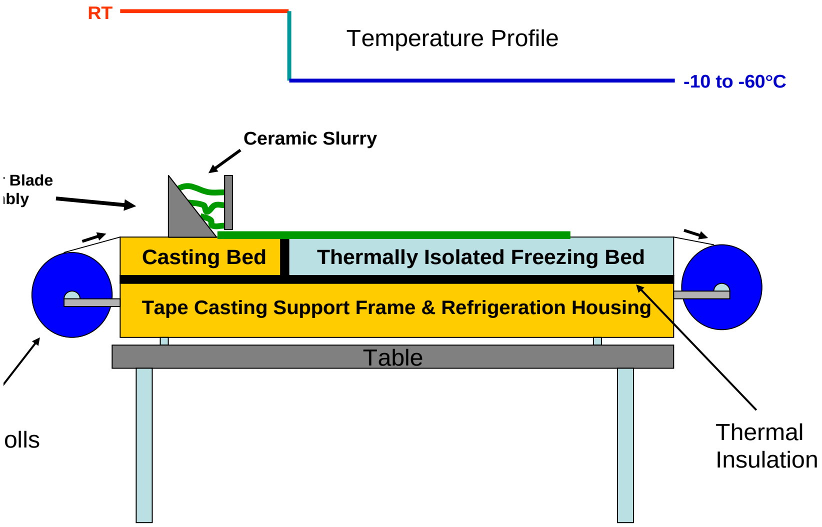

Figure 1. Freeze Tape Casting Apparatus

Task 3 utilized yttrium stabilized zirconia (TZ-8YS, Tosoh) with corn starch added as a pore former at 45wt% to achieve an interconnected pore network. A fully saturated nickel nitrate (Alfa Aesar) precursor was prepared for infiltration. To aid in pore penetration, a pine oil based surfactant (Dynol 604, Air Products) was utilized at 0.25wt% of the water quantity. Nickel nitrate solution was infiltrated, allowed to dry for one hour in a 75°C drying oven, and thermal decomposed at 500°C for subsequent re-infiltration to achieve the proper nickel loading. Infiltrated samples were characterized by electron microscopy to ascertain the extent of nickel metal percolation before and after thermal treatments in reducing atmospheres.

1.4 Results and Discussion

1.4.1 Task 1: Microstructurally Engineered Electrodes

The freeze casting process generates unique pore structures that show a variation in pore morphologies that are shown in Figure 2. These variations were initially regarded as random growth of a tumultuous solidification process due to the short range order of ice crystals forming in the tape, resulting in regions of ordered pores similar to grains. A key processing parameter has been identified through this study of the microstructure control of freeze-tape cast systems that dramatically improves the homogeneity of the pores throughout the tape. While the freeze-tape cast system is designed to generate continuous graded pore structures by the uni-direction solidification of aqueous slips through the thickness, the overall uniformity of the pores is dramatically affected by the pulling speed of the mylar carrier of which the slurry is solidified upon as shown in Figure 3. Initial freeze-tape casting was performed at rates of 10 – 15mm/sec in regards to the mylar carrier pulling speed resulting in randomized regions of ice crystals. Upon close examination of the solidifying tape it was observed that solidification of the tape from front to back could be visually tracked. It was then ascertained that solidification from front to back for the initially cast 1000um thick zirconia tapes approached ~1mm/sec at a freezing platen temperature of -25°C show in Figure 3. At casting rates much greater than the planar solidification rate, regions of the green tape solidified to form large clusters of oriented pores and, hence, boundaries between these clusters as shown in Figure 4. Casting speeds of less than 1mm/sec are effective in producing a single solidification front that propagates from the front to back of the tapes yielding uniform microstructures throughout the entire tape without the intersection of separately growing ice regions.

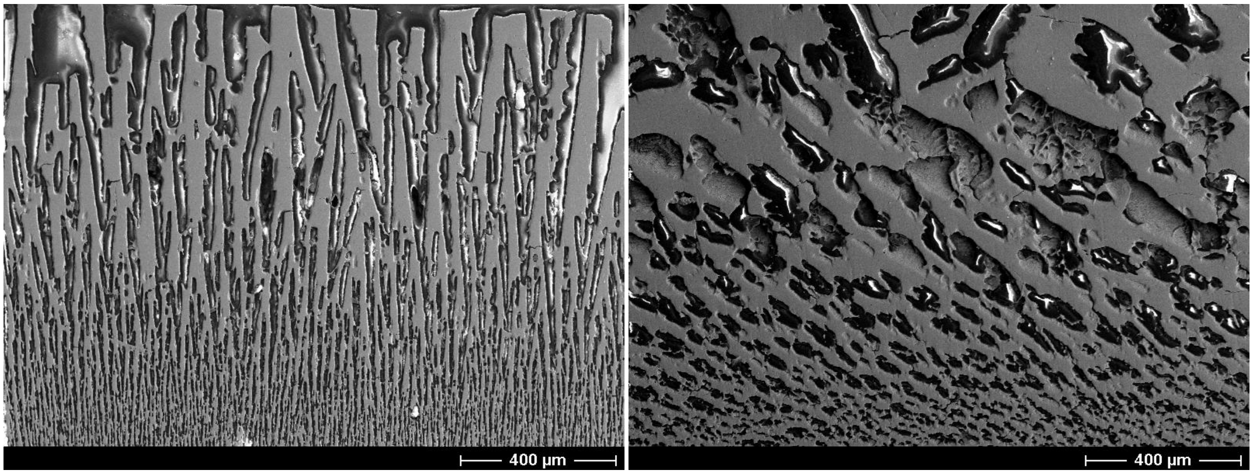

Figure 2. Cross-Section of Freeze Cast Tape
View Parallel to Casting Direction (Left), View Perpendicular to Casting Direction (Right)

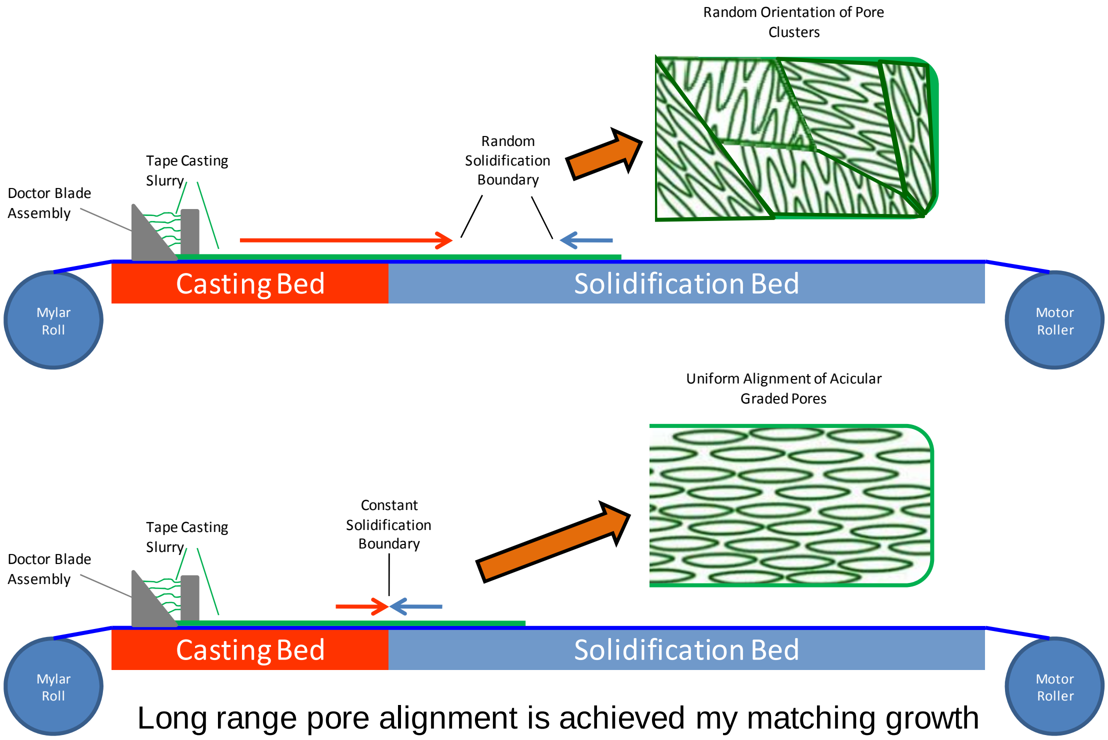

Long range pore alignment is achieved my matching growth rate with casting speed, ~ 0.1 to 0.5mm/sec

Figure 3. Slurry Solidification Giving Rise to Continuous Graded Pore

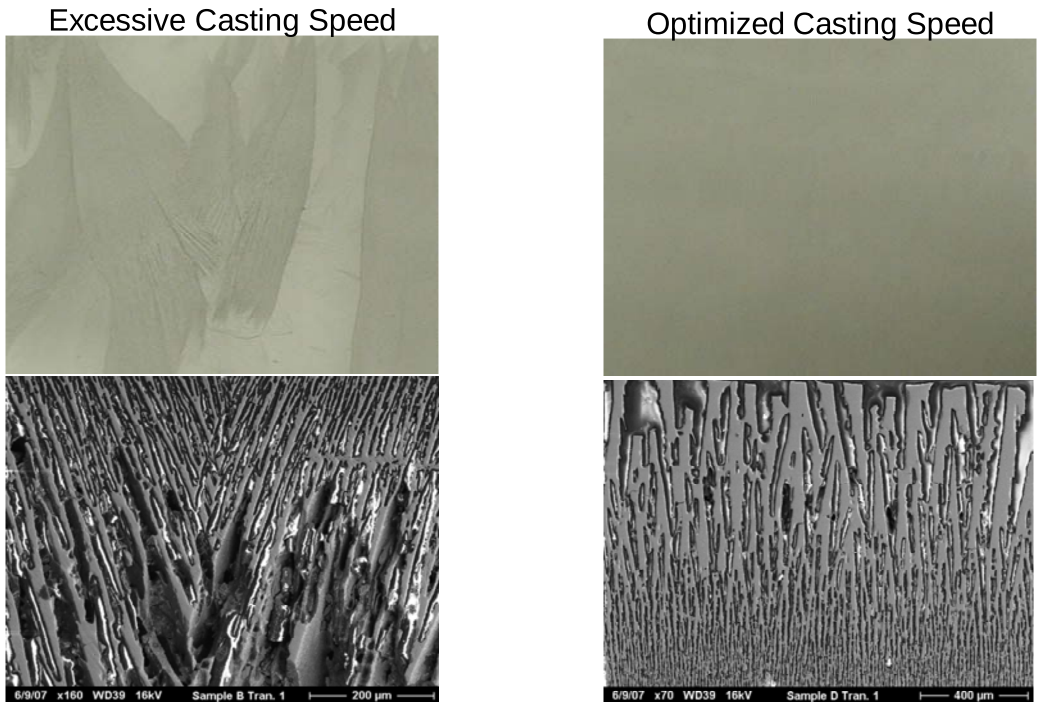

Figure 4. Observation of Tape Surface (Top) and Parallel Viewed Microstructure (Bottom) as a Function of Casting Speed

This new processing parameter yields tapes with minimal local density and morphology variations, ideally suited for preparing up to 2" SOFCs with these microstructures for fuel utilization studies. Utilizing the new freeze casting parameters, the density of sintered zirconia tapes was evaluated as a function of freezing rate and solids loading as shown in Figure 5.

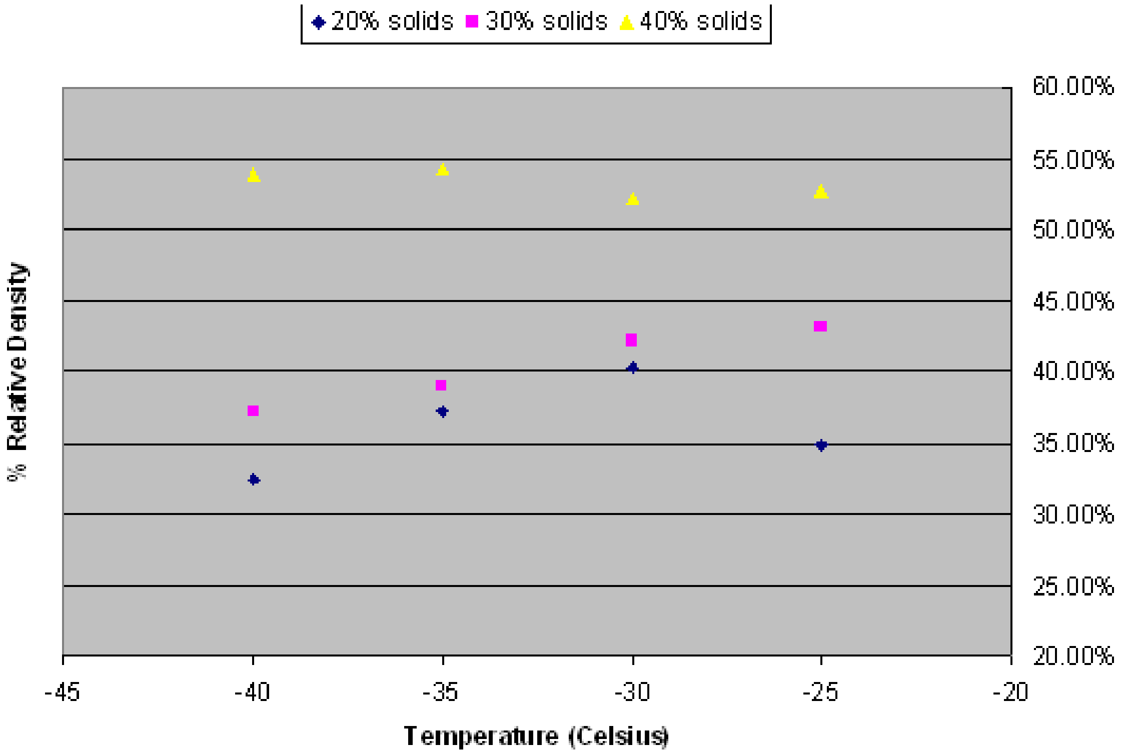

Figure 5. Relative Density of Freeze Cast Sintered Tapes as a Function of Freezing Rate and Solids Loading

It is evident that freezing rate (platen temperature) results in minimal density variation which is driven primarily from localized variation in microstructure and inhomogeneities in the slurry prior to casting. This behavior was anticipated given that the volume fraction of solids is not undergoing change. Increasing freezing rate does, however, yield decreased pore divergence and, thus more columnar pore channels. To prove the concept that the freeze casting process is suitable for anode supported cells fabrication, a 1.5" diameter ASC was fabricated with an approximately 30 micron zirconia electrolyte and 50 micron lanthanum maganate cathode. The performance of the cell is shown in Figure 6.

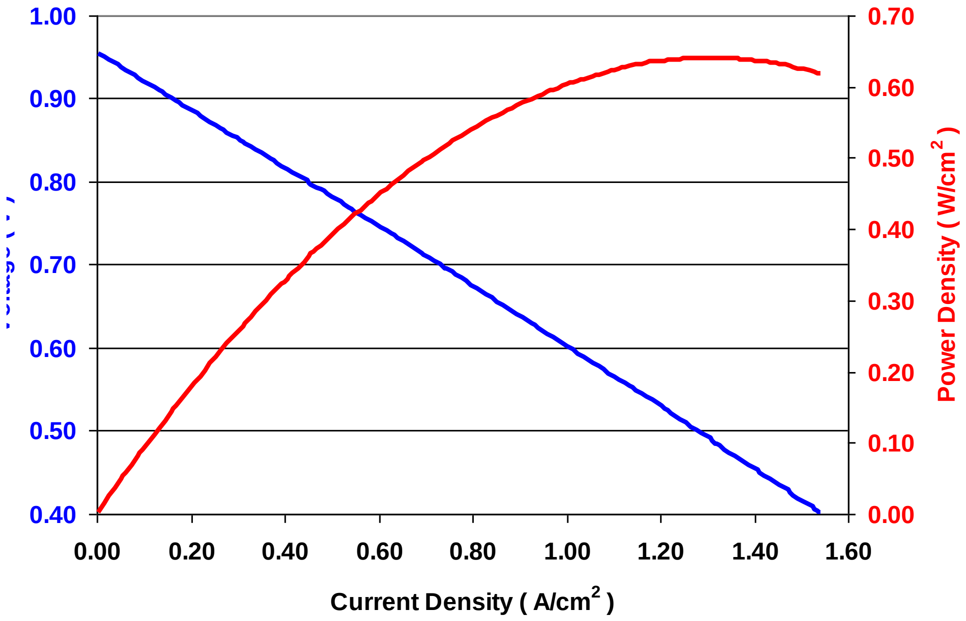

Figure 6. Cell Performance of Freeze Cast ASC at 850°C

A key observation for this cell is that at very high current densities, in regions where concentration polarization is often indicated, the VI behavior of the freeze cast cell remains linear, driven by ohmic losses from ionic resistivity. It is, however, noted that ASCs prepared with nickel/zirconia freeze cast anodes yield relatively poor strength requiring additional development from a mechanical support perspective and as a result, potentially significant stack re-designs for proper implementation.

1.4.2 Task 2: Low CTE Ni/Ceria Anodes

Aluminum titanate filler compound, with a net CTE of 0.5ppm/°C, was mechanically mixed with ceria based anode powders. The thermal expansion of sintered nickel oxide/gadolinium doped ceria/aluminum titanate (NiO/GDC/ALT) sample bars has been evaluated after processing at 1300 and 1400°C for each aluminum titanate concentration as shown in Figure 7. After dilatometry in ambient conditions, these samples were reduced in hydrogen at 800°C for 40 hours to ascertain the thermal expansion coefficient in the reduced state, indicative of an operating SOFC. The CTE of the reduced sample bars is shown in Figure 8.

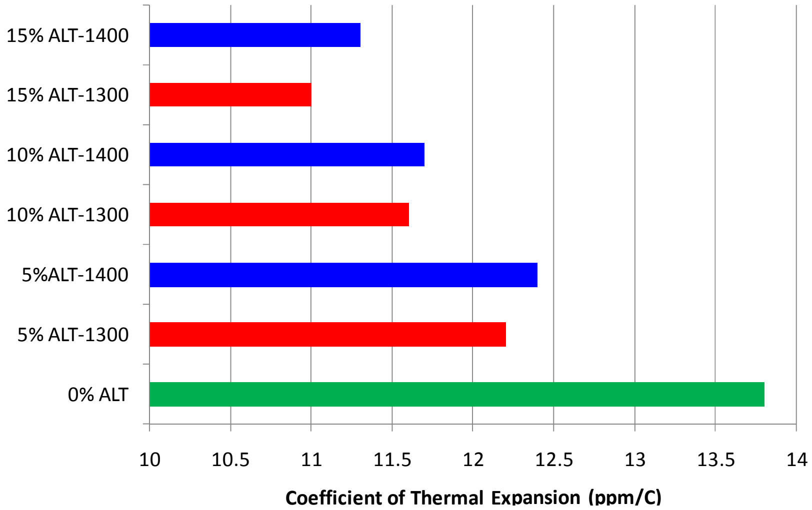

Figure 7. Thermal Expansion of as-Processed (Oxidized) State of Anode Blend Bars

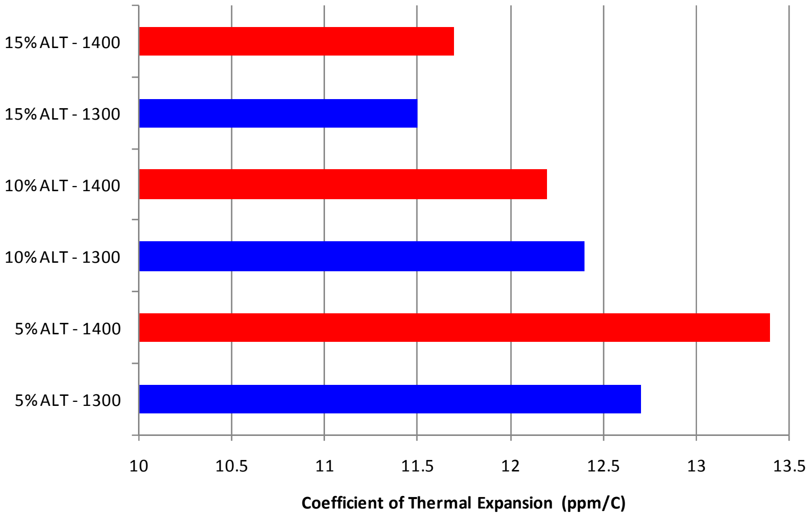

Figure 8. Thermal Expansion of Reduced Anode Blend Bars

It is readily apparent that the aluminum titanate additions yield a nearly linear decrease in CTE, which corresponds well to CTEs predicted by a rule of mixtures model, employing fractional weighting of CTE based on volume of each phase. This indicates a means for the tailoring of anode thermal expansion behavior employing cerium oxide in which the CTE can be readily matched to that of zirconia electrolytes. The 1400°C processed bars show a consistent trend of CTE values greater than the 1300°C bars. This trend indicates that secondary phases may be forming as a result of the decomposition of aluminum titanate. To explore this phenomenon, aluminum titanate was mixed with nickel oxide and gadolinium doped cerium oxide to evaluate the chemical compatibility of the ultra low CTE aluminum titanate filler compound. An SEM micrograph of the pressed pellet sintered at 1400°C for two hours indicated the secondary phase, which was shown to contain Gd and Ti by EDS analysis, shown in Figure 9.

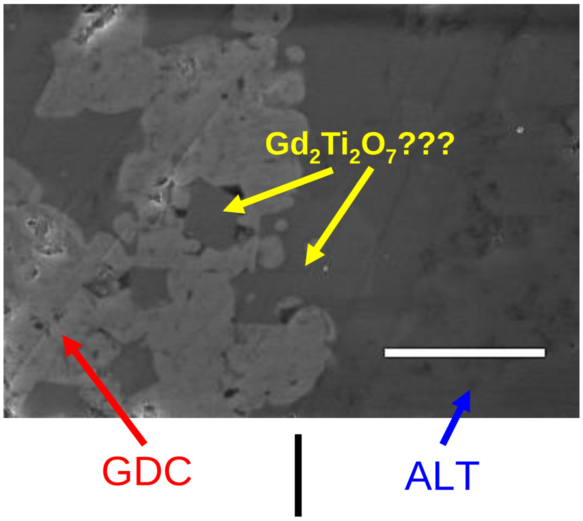

Figure 9. Reaction of ALT and GDC at High Temperature

NiO/GDC/ALT anode batches were also evaluated by XRD analysis. Batches were sintered at both 1300°C and 1400°C. While the GDC densifies very well at 1300°C, the bulk/active anodes in addition to the electrolyte will be sintered at 1400°C; therefore, the compositions were also tested at 1400°C for two hours. The formation of $Gd_2Ti_2O_7$ pyrochlore secondary phase is the most evident, with the minor formation of $NiAl_2O_4$ shown in Figure 10.

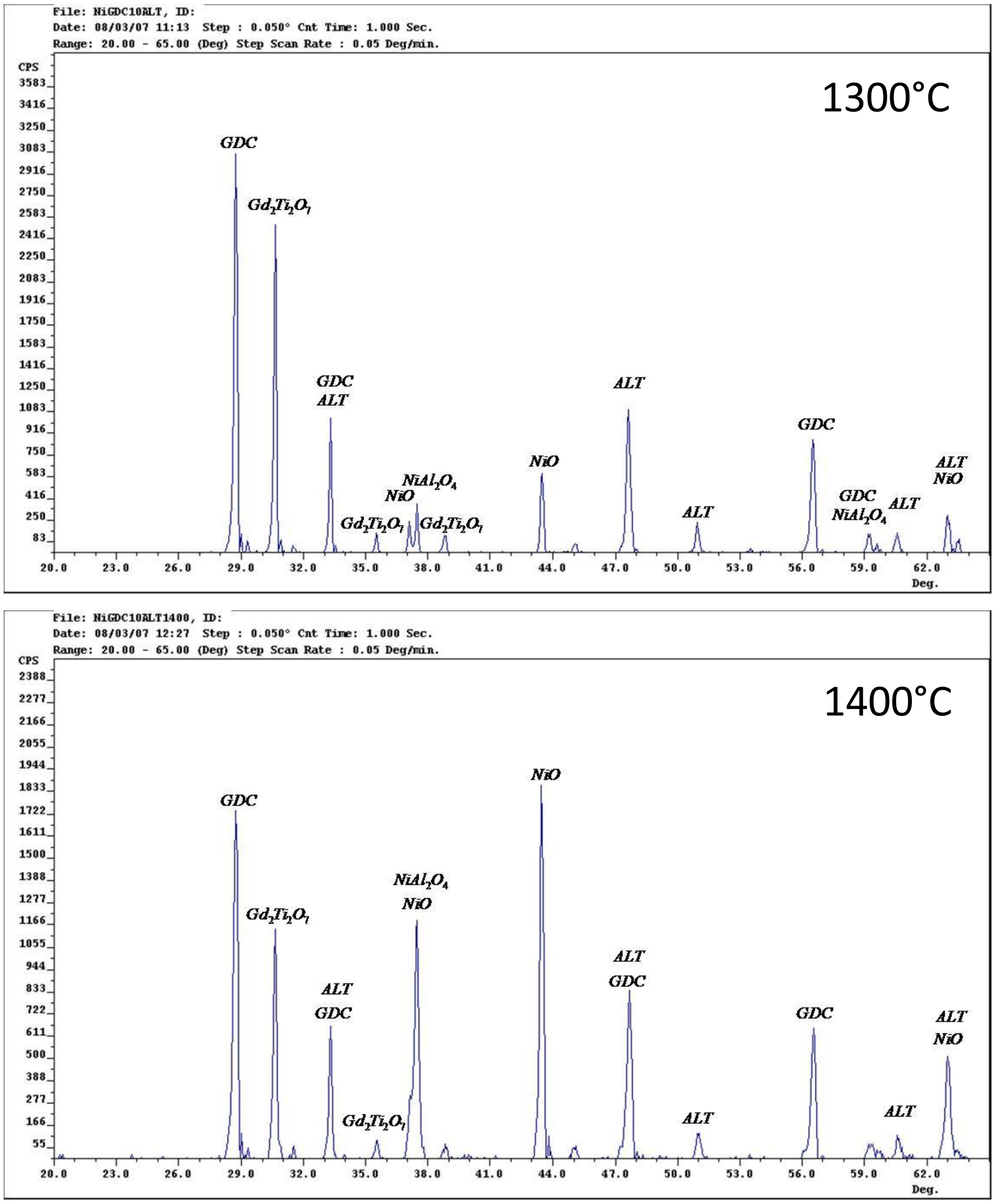

Figure 10. XRD Patterns for NiO/GDC/ALT Sintered for Two Hours

Significant difference between 1300°C and 1400°C samples is not readily evident and the same secondary phases appear to be present. Given the higher temperature, and the dilatometer results, it appears that the higher temperature facilitates more extensive reaction, hence decomposition of aluminum titanate and consequently, mitigating the low CTE filler effect.

The electrical conductivity of the bars was also measured at room temperature to determine the conductivity degradation as a function of ALT addition. These results are shown in Figure 11 and indicate that while additional secondary phase forms in the 1400°C processed samples, it appears to be localized, therefore not affecting the main conductivity pathways in the specimen for current collection. The 5% and 10% dopant blend bars yield excellent conductivity while providing the types of CTE reductions that make using cerium oxide more attractive.

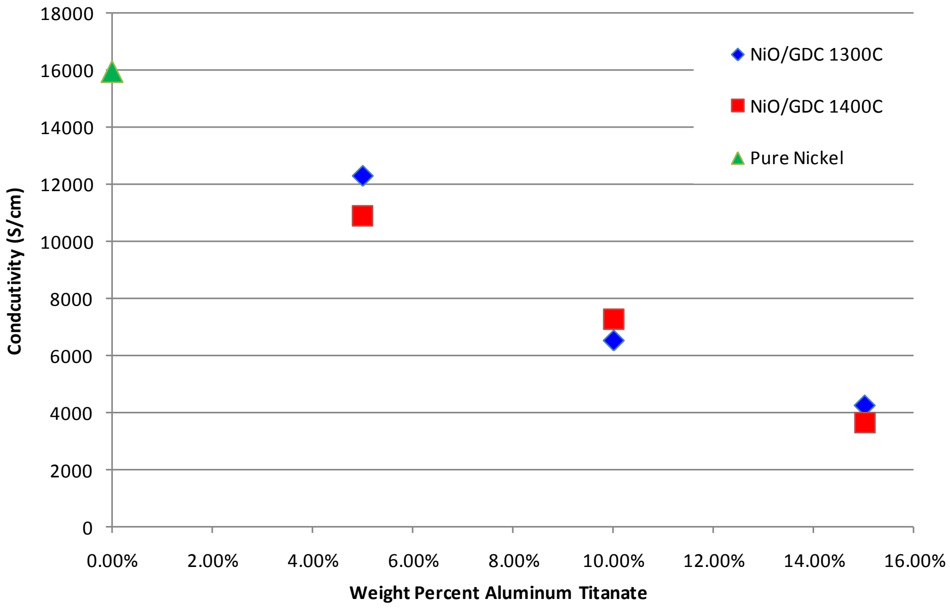

Figure 11. Room Temperature Electrical Conductivity of Reduced Anode Blend Bars

While the initial train of thought suggests that this chemical reaction with ALT/GDC/NiO reaction is undesirable, gadolinium titanate has functional characteristics that may be attractive for SOFC electrode functionality. Furthermore, these secondary phase formations may yield some benefit in improving the mechanical properties of the blends. Simple three point bend tests were performed on a series of sample bars with and without ALT additives employing fine (Black) and coarse (Green) nickel oxide powders, shown in Figure 12. The aluminum titanate dopant indicates a significant improvement for both the coarse and fine nickel oxide powders; however, no direct correlation can be ascertained with regards to the mechanical characteristics of the nickel oxide particle size. The mechanical characteristics of the reduced sample bars, on forthcoming tests, may however yield a different trend.

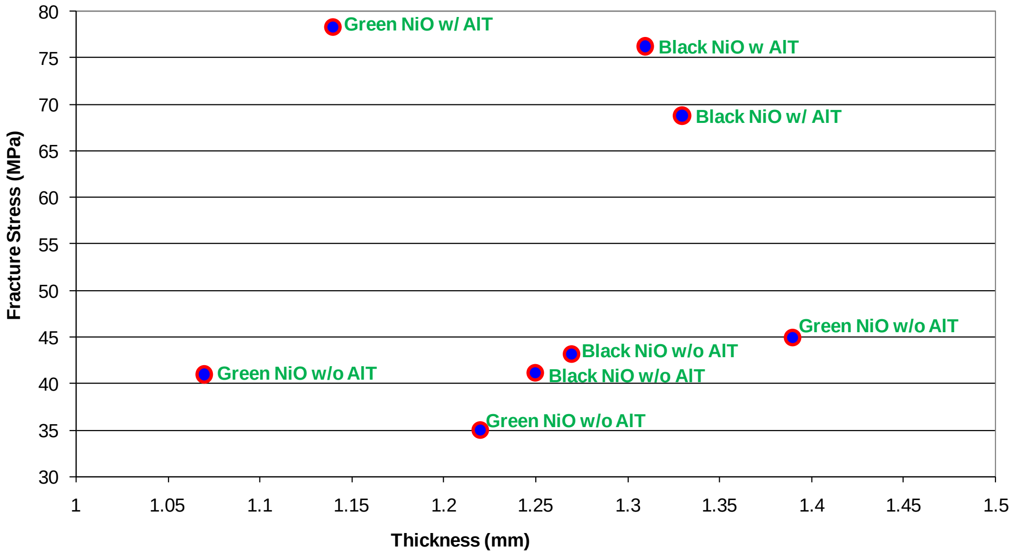

(as Sintered, Oxidized State)

1.4.3 Task 3: Solution, Slurry, and Vapor Infiltration of Active Electrodes

Complete infiltration of nickel electrode on an YSZ scaffold is the primary focus of this activity, which is aimed at addressing the migration of nickel catalyst from thermal treatment in a reducing environment. Figure 13 illustrates the deleterious effects of nickel migration during thermal treatment in which smaller, more catalytically active particles facilitate accelerated coarsening. Infiltrated nickel electrodes can, therefore, rapidly lose their percolated structure and, hence, essential current collection capability.

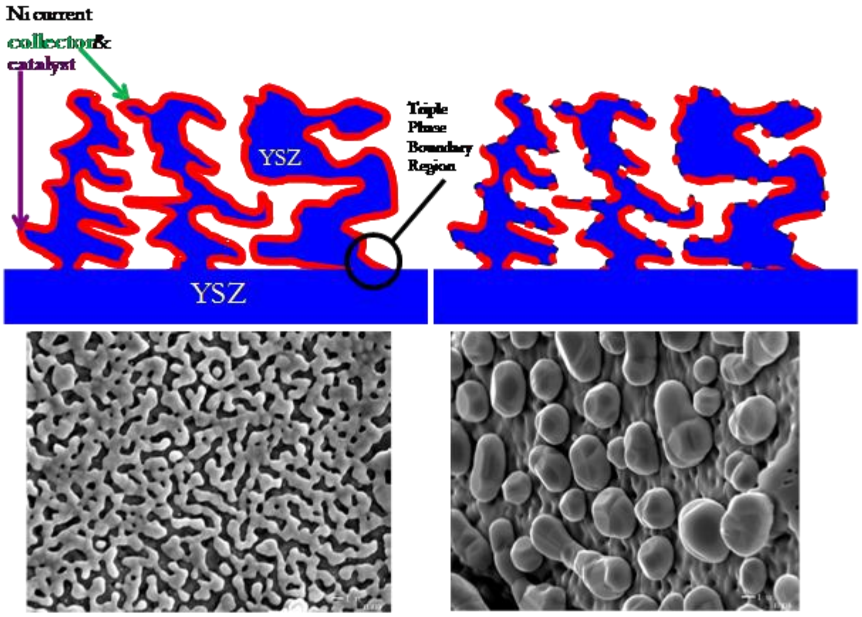

Figure 13. Infiltration of Anode n YSZ Scaffold Approach and Thermal Degradation Effects

To evaluate a means of anchoring the nickel anode network in place, additions of aluminum titanate have been added to the YSZ scaffold to introduce sites for which the nickel anode may remain attached during cell operation. Graphite flake, carbon spheres, and corn starch were utilized as a thermal fugitive pore former; however, based on microstructure in Figure 14, the corn starch yielded the most suitable structures for infiltration.

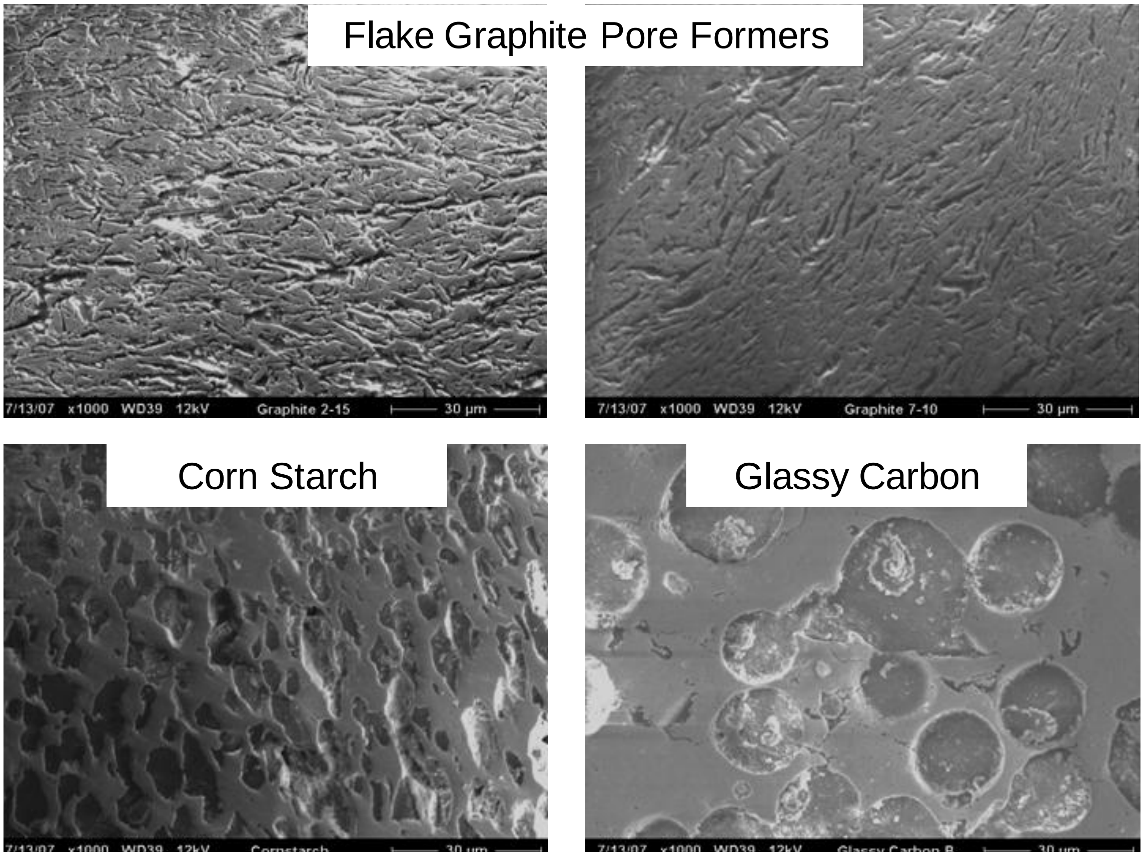

Figure 14. Pore Former Morphologies after Sintering

To insure ample porosity for infiltration, 45wt% corn starch was added to YSZ for preparation of the anode scaffolds. Anchoring ALT dopants were also added to the YSZ/corn starch mixture to induce anchoring sites for the nickel anode network in quantities of 5wt%. Samples were sintered at 1400°C for two hours and infiltrated under a vacuum to ensure complete solution penetration. YSZ porous microstructures utilizing 45wt% corn starch pore former were infiltrated with a fully saturated nickel nitrate/water/surfactant solution for a total of five cycles. After infiltration, samples were allowed to dry for one hour at 75°C in a convection drying oven and then the nitrate was decomposed at 500°C prior to the subsequent infiltration step. YSZ samples doped with aluminum titanate were additionally heated to 1300°C for one hour to facilitate the formation of chemical anchors prior to reduction. Five independent samples with and without 5wt% aluminum titanate dopant were utilized for the study. The aluminum titanate dopant appears to act as a sintering aid to some degree and densities of the doped pellets were substantially higher than the densities of the undoped YSZ. The concentration of nickel deposited after five infiltration cycles is shown in Figure 15.

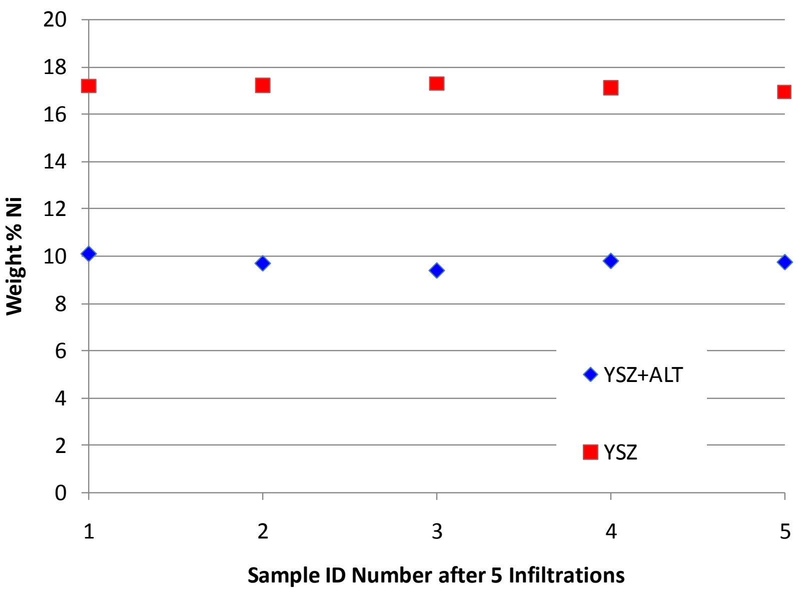

Figure 15. Nickel Content after 5 Infiltrations for Baseline YSZ and with Alt Dopant

The reduced density of the ALT doped specimens is evident from the level of infiltrated nickel; however, all samples achieved at least 10wt% to yield a well interconnect network of nickel. Furthermore, the infiltration process shows excellent consistency for achieving targeted nickel loading.

To ascertain microstructural evidence of aluminum titanate induced chemical anchoring, pellets with five infiltrations (with and without ALT) were cleaved in half with one half undergoing low temperature reduction to ascertain the as reduced microstructure while the other half undergoing 72 hours of reduction at 800°C to ascertain the effects of nickel coarsening. The as reduced samples are shown in Figure 16, yielding microstructures that are nearly identical.

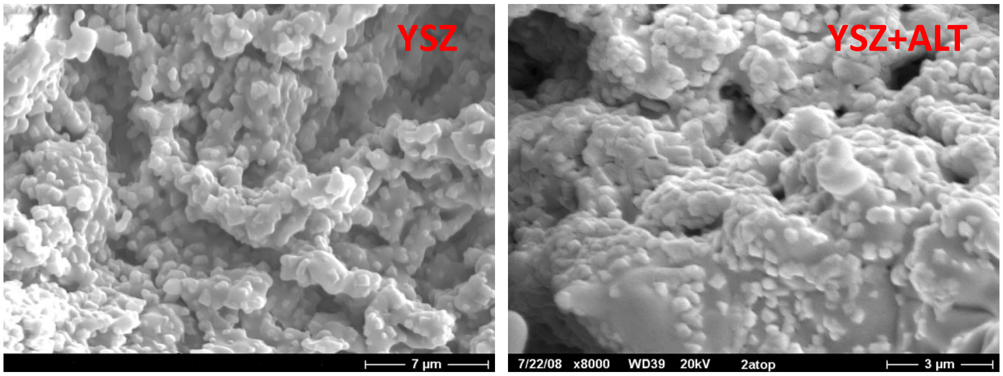

Figure 16. As Reduced Microstructure after 5 Nickel Nitrate Infiltrations

The microstructures shown from samples in Figure 17 indicates substantial coarsening after only 72 hours, which is anticipated given the sub-micron size of the metallic particulate. The metal microstructure in the samples without ALT dopant show increased nickel agglomerate size in addition to separation of the nickel network.

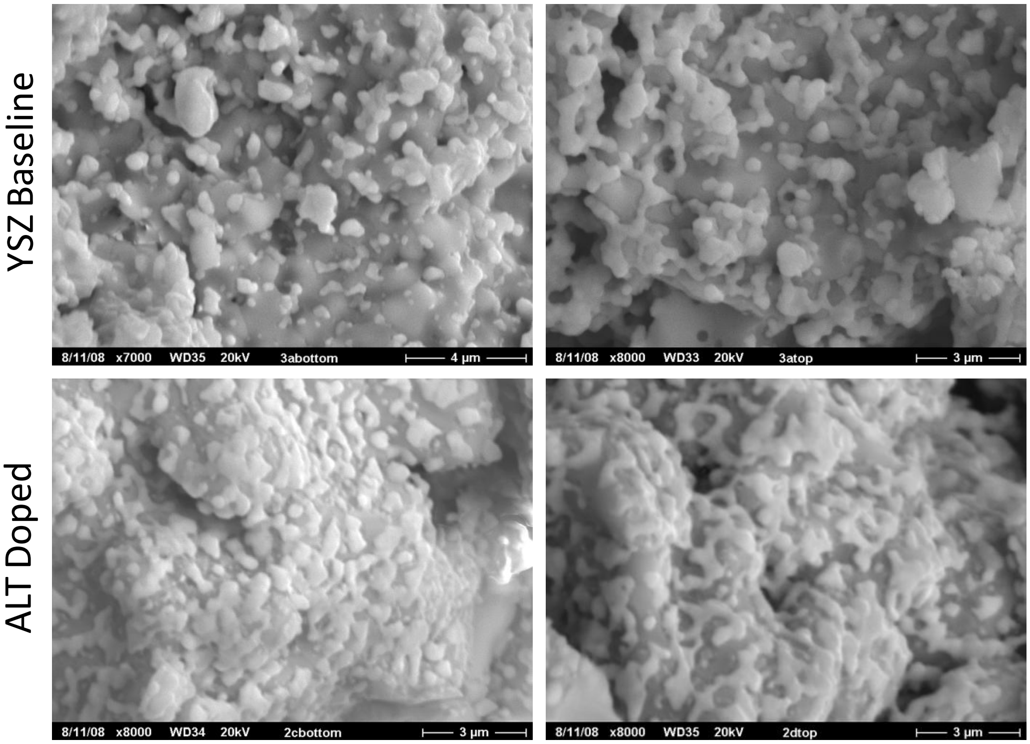

Figure 17. Microstructure after 72 Hours Reduction at 800°C

The samples doped with ALT shown a more contiguous nickel network with less separation of discrete nickel clusters. To further explore the affects of the aluminum titanate anchors, a new sample set of infiltrated Ni samples were thermally treated for 150hrs at 800°C. These samples were prepared discrete form the initial 72hr study to provide a secondary set of data and establish repeatability in processing. Infiltration of the ALT doped and undoped specimens yielded nearly identical nickel concentration after five concurrent infiltration cycles. The effects of nickel coarsening are readily evident in Figure 18 in which the nickel metal has a smooth surface finish as opposed to the rough surface finish of the as reduced and even 72hr treated specimens. The nickel catalyst coating, however, appears to remain continuous, porous, and adherent to the YSZ porous scaffold.

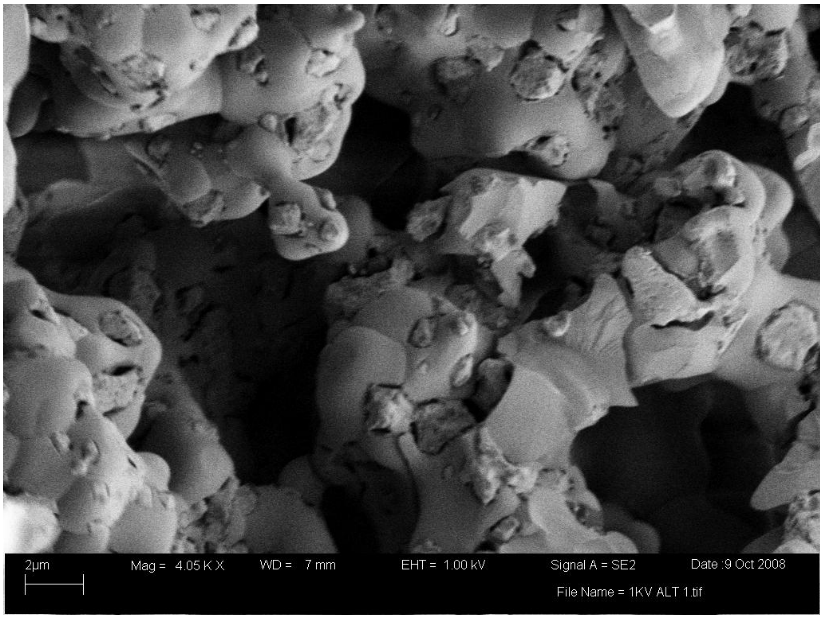

Figure 18. Microstructure of Alt Doped Nickel Infiltrated YSZ Scaffold Subjected To 150hrs Thermal Treatment in Hydrogen at 800°C

High resolution imaging of the undoped infiltrated YSZ scaffold was not readily attainable due to charging during imaging. This indicates a breakdown of the conductive nickel network and the low resolution image of the undoped specimen in Figure 19 shows some separation of the nickel metal from the scaffold supporting this hypothesis.

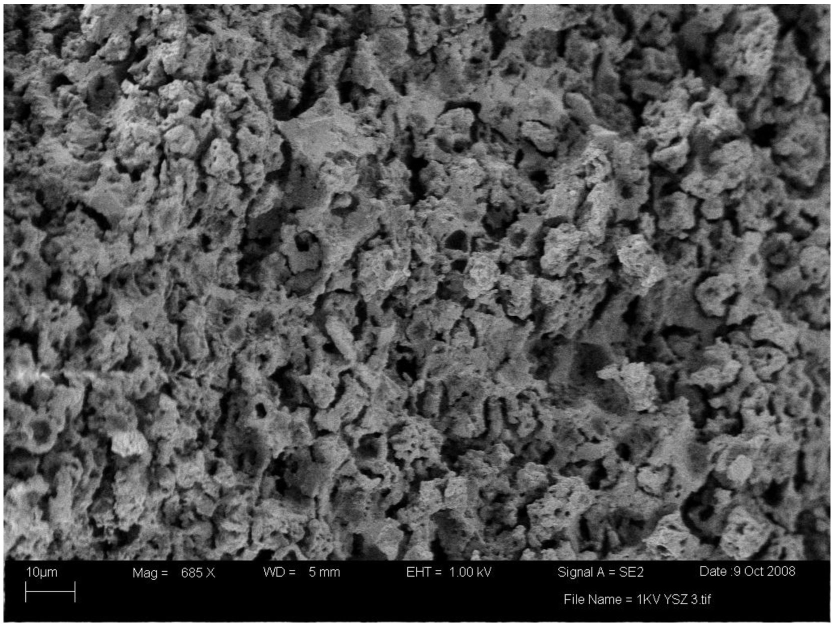

Figure 19. Microstructure of Undoped Nickel Infiltrated YSZ Scaffold Subjected to 150hrs Thermal Treatment in Hydrogen at 800°C

X-ray Diffraction (XRD) analysis was utilized to determine the temperature at which secondary phases formed. The order of reaction in which these new phases generate chemical anchors are shown in Figures 20-22. XRD patterns of anode powder blends [(66wt% NiO + 34wt%YSZ)

+30% ALT] in Figure 20 were acquired after sintering the compacted powder blends at 1400°C with no post reduction step. The XRD scans showed the presence of two new phases, nickel aluminate (NiAl2O4) and zirconium titanate (ZrTiO4). The formation of NiAl2O4 indicates the reaction of Al2O3 and NiO as well as the reaction of TiO2 and YSZ in the formation of ZrTiO4. ALT is not detected in the scans suggesting near complete reaction of the compound. It is apparent that the ALT decomposes into Al2O3 and TiO2, which may be catalyzed by the presence of NiO and YSZ.

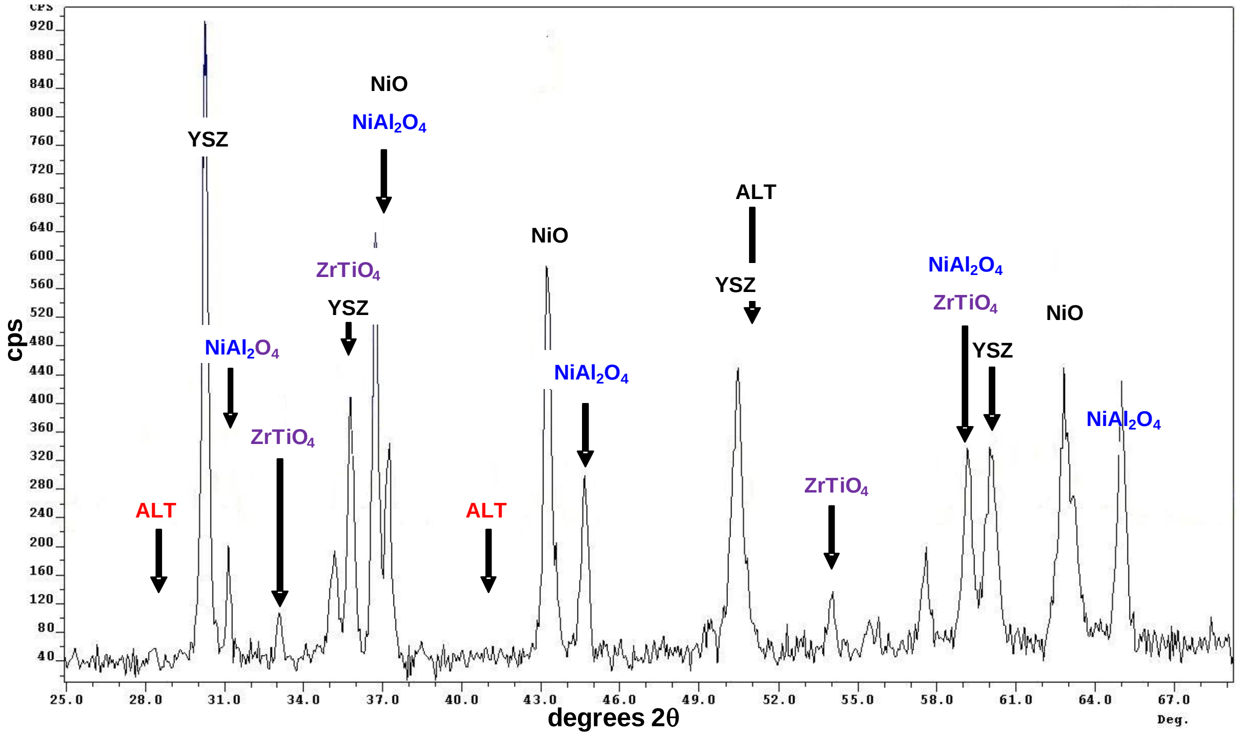

Figure 20. XRD Pattern for ALT/YSZ/NiO Sintered at 1400°C

It is well understood that ALT is thermodynamically unstable between 900°C and 1200°C. Figures 21 and 22 indicate the order in which the secondary phases form. It is seen that the NiO/ALT powders reacted as low as 1100°C to yield NiO+Al2O3=>NiAl2O4, whereas the ALT/YSZ powders required a temperature of 1300°C before the two constituents reacted to yield YSZ+TiO2=>ZrTiO4. This is representative that the ALT/YSZ interaction requires greater thermal energy to decompose the ALT into its constituents, which is believed to occur after the NiO facilitates the formation of aluminum oxide.

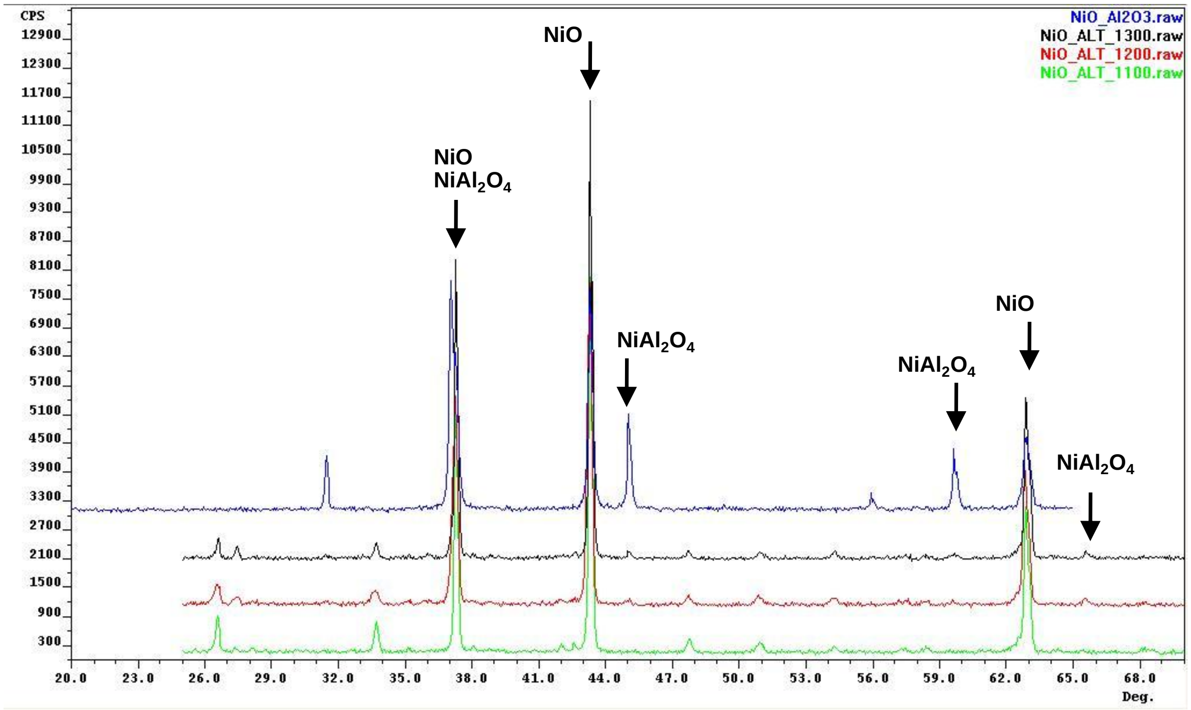

Figure 21. NiO and ALT Sintered to 1100, 1200, and 1300°C and Compared with NiO and Al2O3

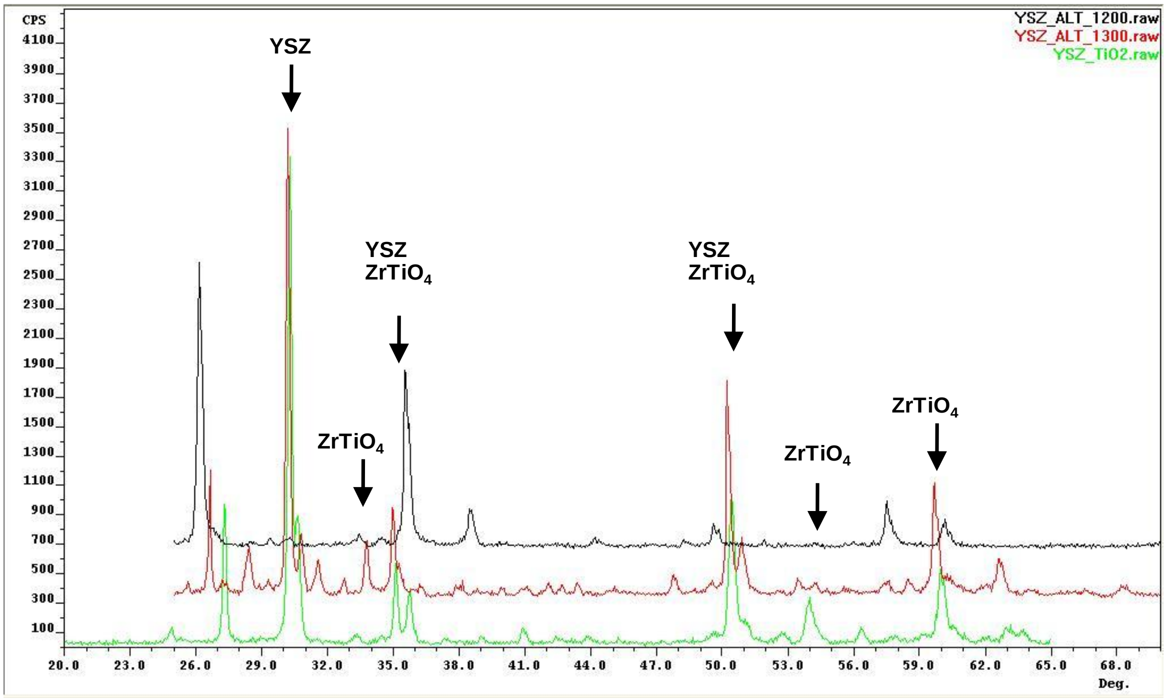

Figure 22. YSZ and ALT Sintered to 1200 and 1300°C and Compared with YSZ and TiO2

The formation of minor quantities of ZrTiO4 and NiAl2O4 appear to provide a mechanism of chemically anchoring the Ni network and YSZ scaffold in a manner depicted in Figure 23.

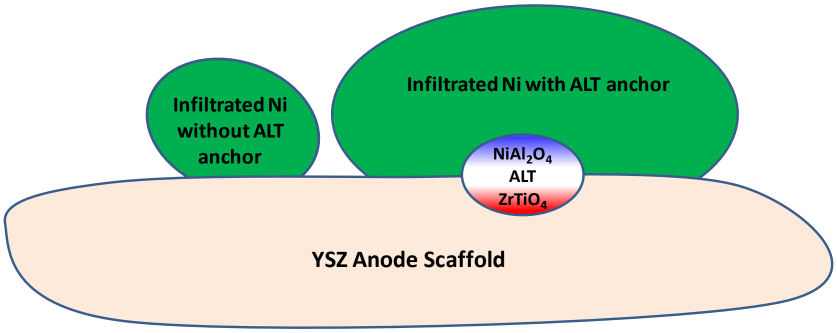

Figure 23. Schematic of Chemical Anchor Formation Based X-Ray Diffraction and SEM Analysis

1.5 Conclusions

Freeze tape casting has been shown to be effective in fabricating anode supports with excellent gas diffusion characteristics. Processing modifications have generated the capability to fabricate large area anode substrates for ASC fabrication. Freeze cast based ASCs have demonstrated >600mW/cm2 performance with negligible concentration polarization, resulting in linear VI curves in the high current density regions. The strength of freeze cast substrates does, however, present an immediate limitation for implementing this cell technology in applications requiring robust cells. Further efforts are needed to identify methods of improving mechanical properties while optimizing electrochemical performance.

Aluminum titanate has shown to be an effective dopant for reducing the CTE of nickel oxide/cerium oxide based high performance anodes. Effective CTE reductions near that of the zirconia electrolytes can be achieved with 10-15% ALT additions while retaining 50-75% of the baseline nickel conductivity. Both CTE and conductivity yield linear trends, and are well approximated with a rule of mixture model. The effect of secondary phase gadolinium titanate is not clear and electrochemical/impedance testing is further required to understand the impacts of the dopant with respect to electronic conductivity, ionic conductivity, and catalysis. Further, the effects on strength are not fully understood and require further detailed examination.

The complete infiltration of nickel metal catalysts for SOFC anodes has been demonstrated utilizing in-situ anchoring compounds to facilitate chemical bonding between the porous zirconia scaffold and percolated nickel network. Aluminum titanate is shown to facilitate the stepwise formation of nickel aluminate, followed by zirconium titanate. Chemical anchors have shown effective in mitigating nickel catalyst coarsening based on nitrate solution infiltration. The extent of remaining ALT and interface between NiAl2O4 and ZrTiO4 remains to be established quantitatively for which detailed examination is continuing. DC conductivity and impedance testing is necessary to further establish the affects of the anchors on electrochemical performance.

2.0 HIGH PERFORMANCE, HIGH POWER DENSITY SOLID OXIDE FUEL CELLS LOAD CONTROL

2.1 Summary

The focus of this report is to address the proper matching of components in a solid oxide fuel cell (SOFC) powered unmanned aerial vehicle (UAV) propulsion system with the goal of optimizing the efficiency of the system given the design constraints of the UAV. Previous research regarding fuel cell powered UAVs has primarily come from the aerospace industry with one team declaring the most important consideration to be the matching of the motor and propeller used in the propulsion system to the characteristics of the fuel cell used as the power source. Based on that conclusion, this report presents a physically-based model for design and optimization of a fuel cell powered electric propulsion system for an UAV.

The major components of such a system, the fuel cell, the motor, the motor controller, and the propeller, are introduced and described in detail along with their associated physically based models used in the simulation program. The simulation program combines and numerically solves these models finding an overall solution vector which details the operation of each system component. Using this simulation program, a graphical procedure is presented allowing easy assessment of combinations of system components and identification of the most practical and efficient combinations.

To verify the component models and simulation program, an open circuit wind tunnel was constructed to simulate flight conditions for testing of our system components. Several different AXI brand brushless direct current (BLDC) motors, the DBL 5330, the 5345-16, the 5345-18, and the 5360 were tested in conjunction with four APC brand electric motor propellers, the 22 in. x 12 in., the 24 in. x 12 in., the 26 in. x 15 in., and the 27 in. x 13 in. The simulation model was used to determine the most optimal combinations of system components for a given fuel cell model. Based on these results, experimental data was collected in the wind tunnel detailing the operation of one of these optimal configurations, the AXI 5345-18 motor and the APC 27 in. x 13 in. propeller. This data generally shows good agreement with the performance of the system predicted by the simulation program.

The report concludes that the simulation model presented provides good indication as to the performance of the components in question and thus, is an important tool in propulsion system design. Additionally, the graphical procedure eases the coordination of multiple groups involved in building the fuel cell / electric propulsion system as the implications of altering the characteristics of the fuel cell and propulsive components are easily identified.

Finally, the report recommends continued testing of propulsive components with an emphasis on the propeller model and the effects of wind tunnel blockage on accuracy of thrust measurements. In regards to future research, the report recommends considering the implications of a secondary power source and enhancing the simulation program with dynamic models for system components.

2.2 Introduction

Fuel cells have received increasing interest for their ability to effect efficient, quiet, and clean conversion of chemical to electrical energy. These attributes also make fuel cells an attractive power source for electric propulsion in UAVs. Potential advantages of fuel cell / electric UAV propulsion include decreased emissions, increased efficiency, increased range and loiter time, and quieter, lower profile flight.

Previous efforts in fuel cell powered UAVs have primarily come from the aerospace community. Ofoma and Wu [1] provide a fuel cell UAV study based on environmental research needs, while Soban and Upton [2] describe a scheme for narrowing the classes of UAVs best suited for fuel cell propulsion. In the Moffitt, Bradley, Parekh, and Mavris publication [3], a team at the Georgia Institute of Technology performed a full system design and optimization of a proton exchange membrane (PEM) fuel cell UAV. The authors [3] suggest that matching motor and propeller to the characteristics of a given fuel cell is the most important aspect of a successful design.

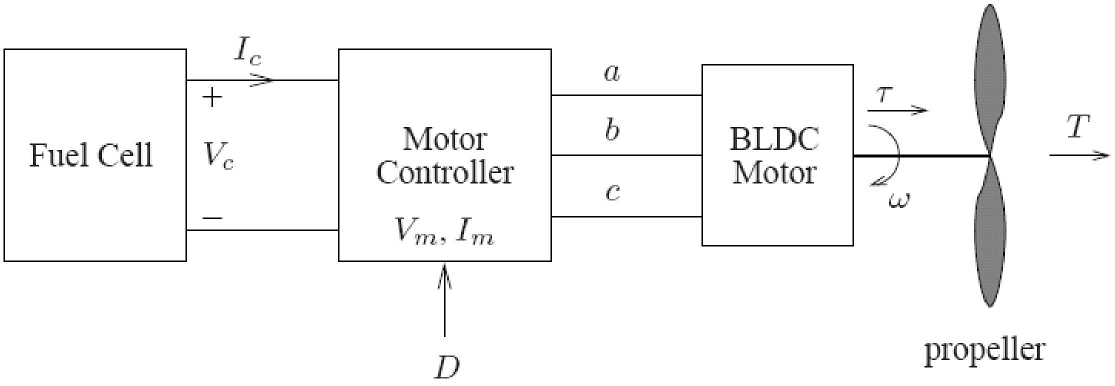

Figure 24. System Diagram
Block Diagram of Fuel Cell Powered UAV Electric Propulsion System

This report considers the steady-state modeling, design, and component selection for a solid oxide fuel cell (SOFC) powered electric propulsion system, as suggested by the block diagram in Figure 24. In particular, we are concerned with optimizing the delivery of power from the fuel cell terminals to the propeller. In the methods, assumptions, and procedures section, first-order mathematical models are provided for each of the components in the propulsion system along with information corresponding to the components used in the experimental validation of the models. Additionally, the wind tunnel and propulsion system test stand built in our laboratory for this experimental validation and our methods for collecting data are described. The results and discussion section details both the simulation results, which provide a graphical solution approach that allows easy assessment of design choices, e.g. changing stack specifications, and the experimental results used to verify the simulation models. Finally, conclusions considering the work to date are drawn and recommendations for future work are speculated. A list of acronyms, abbreviations, and symbols used in this report is provided for reference following the references.

2.3 Methods, Assumptions, and Procedure

2.3.1 System Model

The primary purpose of our simulation model is to explore the performance implications of different fuel cell performance characteristics, operating points, and component choices for the motor and propeller in the block diagram in Figure 24. To accommodate various component models, we maintain explicit modularity in the program codes which is mirrored in the descriptions of components in the following paragraphs. We combine these models numerically by finding an overall solution vector,

$$(I_C \quad V_C \quad I_m \quad V_m \quad \omega \quad \tau \quad T)$$

the components of which are detailed in the descriptions of each subsystem, below. The elements of this solution vector can be constrained in the simulation; and there is a one-to-one correspondence between the simulation quantities and measurements available in the lab test setup.

The following sections provide mathematical models and descriptions of the corresponding physical components used in our test stand.

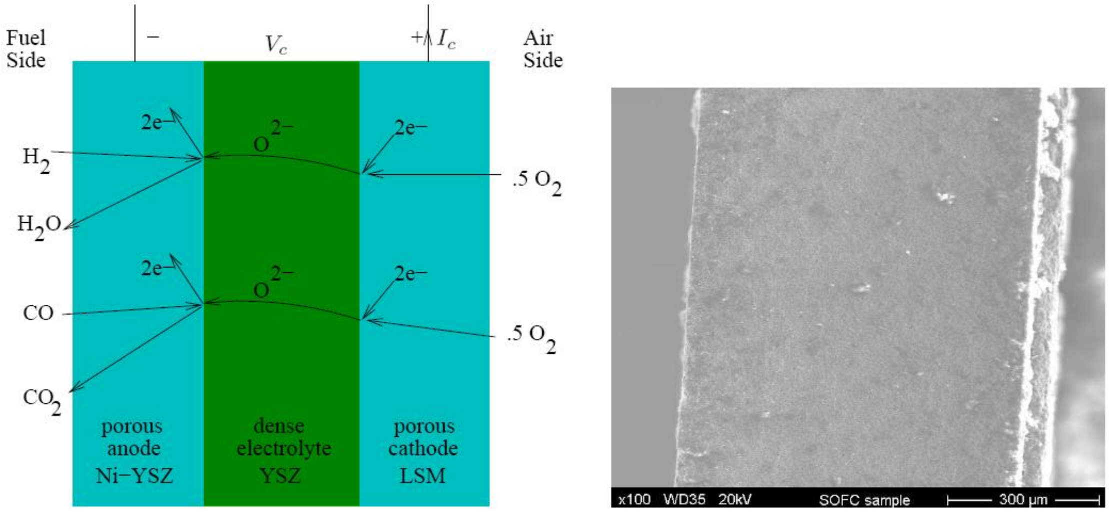

Figure 25. Solid Oxide Fuel Cell Diagrams
Cross-sectional Conceptual Diagram and Scanning Electron Micrograph of a SOFC

2.3.1.1 Solid Oxide Fuel Cell

Figure 25 shows conceptual and actual images of an SOFC. The SOFC is a layered structure consisting of a porous anode, dense electrolyte, and porous cathode. Fuel cells convert chemical energy, stored in a hydrocarbon fuel such as S-8, to electrical energy by essentially partitioning the chemical reaction that would occur in ordinary combustion. Oxygen acquires electrons from the external circuit in the porous, electrically conductive cathode as shown in Figure 25. The resulting oxygen ions diffuse readily toward the reducing atmosphere at the anode by means of oxygen vacancies in the lattice of the electrolyte. The electrolyte has a low electronic conductivity. Oxygen ions arriving at the anode combine readily with processed fuel constituents and give up electrons to the external circuit. The result of this energetically favorable process is direct conversion of chemical to electrical energy, without the efficiency implications of a heat engine.

The scanning electron micrograph (SEM) image in Figure 25 of an anode supported cell provides some indication of the actual scale of a fuel cell structure. The anode appears on the left of the SEM image. The thickness of the anode provides structural support. The electrolyte and cathode appear on the right margin above the scale bar.

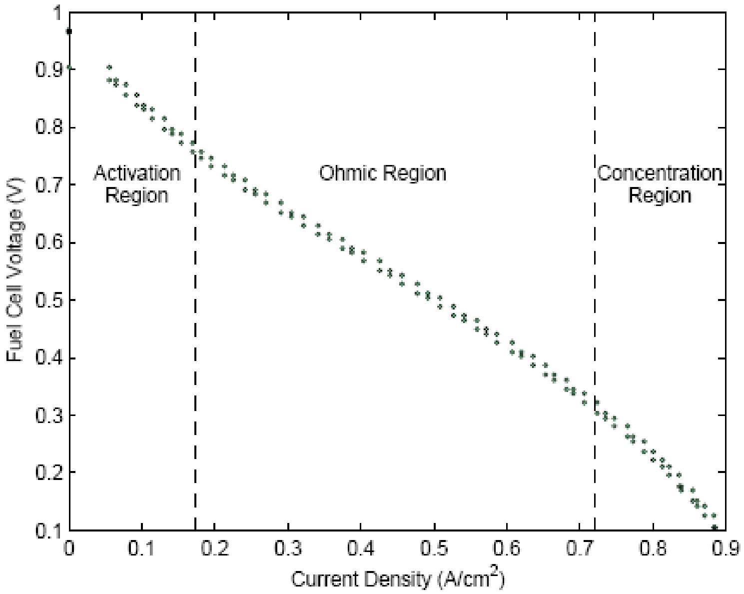

Figure 26. SOFC Polarization Curve Measured Current-Voltage Relationship of A Typical InDEC Anode Supported SOFC

Figure 26 shows measured data representing the current voltage relationship of a typical anode supported fuel cell. The data in Figure 26 is for an InDEC anode-supported cell with an active area of 18 cm^2, at 750 ±°C, operating on oxygen and hydrogen in our laboratory. Individual cells are typically "stacked", or connected in series, to form a power source with convenient output voltages. The response of a stack is like that of an individual cell, except the voltages are higher. In the UAV application, it is reasonable to assume that the stack will be designed under a weight constraint so that the nominal operating point is near the peak power point in the ohmic region of the fuel cell curve. In the ohmic region, the fuel cell can be approximated by a Thevenin circuit equivalent, i.e.

$$V_c = V_{oc} - I_c R_{th} \tag{1}$$

where V_{oc} is the zero-current voltage intercept of the linear approximation of the ohmic part of the response, and R_{th} is the slope. More information on fuel cell modeling can be found in [4–6].

We used a 10 kW Sorenson DCR 160-62T power supply in combination with a resistor built from a variable-length of 6.4 mm diameter 316 stainless steel tube to recreate fuel cell IV characteristics at power levels in the laboratory. A Miller Coolmate 4 welding torch cooling system rated for 4.4 kW was used to stabilize the temperature (and; therefore, the resistance) of the stainless steel by circulating a low-conductivity coolant through the tubing. Typical values of V_{oc} and R_{th} provided by our stack development partners ranged from 50 V to 75 V and 250 mΩ to 600 mΩ, respectively.

2.3.1.2 Brushless DC Motor

Brushless direct current (BLDC) motors feature high efficiency, ease of control, and astonishingly high power density at reasonable shaft speeds [7]. In general, BLDC motors outperform conventional permanent DC motors with better speed and torque characteristics, efficiency, longer operating lives, and increased reliability [9, 10]. These features make BLDC motors a natural choice for electric propulsion of small craft. BLDC motors are permanent magnet synchronous motors, which from a modeling standpoint and are similar to conventional permanent magnet DC motors [8]. The salient difference is that the BLDC motor is commutated externally by power electronic switches rather than by the brushes and commutator built into a standard DC motor. This introduces some electronic complexity, as an external controller is required to switch three phases of windings according to a real-time estimate of the rotor position. For steady-state modeling purposes, we ignore the modeling complexity of the BLDC controller and treat the motor and controller "as commutated", i.e. we assume the controller works as intended, and treat the system as an ideal DC machine with current I_m, voltage V_m, and resistance R_m. The equations describing the motor are then

$$V_m = K\omega + 2R_m I_m \tag{2}$$

$$\tau_e = K I_m \tag{3}$$

where K is the motor speed constant, ω is the shaft speed, τ_e is the torque of electric origin, and R_m is the winding resistance. Values for K and R_m are typically supplied by the manufacturer. Note that R_m appears with a factor of two in this equation because of the convention used in measurement. Motor manufacturers also typically provide current I_0 and voltage V_0 data under "no-load" conditions. We incorporate this data as a windage loss by calculating a drag coefficient

$$\beta = \frac{K^2 I_0}{V_0 - 2R_m} \tag{4}$$

which modifies the output torque τ to ensure that the motor model passes through the specified no-load operating point, i.e.

$$\tau = \tau_e - \beta\omega \tag{5}$$

The net mechanical output is torque τ at speed ω.

Several motors made by AXI were selected for evaluation in the test stand. These motors advertise efficiencies in excess of 90% at the power levels required and have speed constants in a range which does not require a gear box between motor and propeller. Parameters for the motors are listed below. The values for I_0 correspond to $V_0 = 30\ V$.

Table 1. Motors Tested
List of the Motors used in the Study and their Characteristics used in the Simulation Model.

Motor	*K [Vs/rad]*	*R_m [Ω]*	*I_0 [A]*
AXI 5330 DBL	0.041	0.012	4.8
AXI5345-16	0.049	0.017	2.1
AXI 5345-18	0.056	0.021	1.6
AXI5360	0.080	0.034	1.8

2.3.1.3 Motor Controller

In addition to switching the output transistors with rotor position, which is lumped with the model motor, the motor controller can introduce a duty cycle D in the pulses applied to the motor windings. The duty cycle is the input to the propulsion system allowing flight control to change power delivered to the prop. From the power electronics perspective, the average motor voltage over a commutating sequence is modulated by D, so the duty cycle effectively introduces an integrated buck converter. Assuming the converter is lossless, the equivalent voltage V_m and current I_m at the motor terminals are given by

$$V_m = DV_c \tag{6}$$

$$I_m = \frac{1}{D} I_c \tag{7}$$

where D is the duty cycle and V_c, I_c are the fuel cell voltage and current. Losses in the motor controller are neglected because we estimate that they are on the order of 10 W while the motor is drawing in excess of 1 kW.

For laboratory testing we used Jeti Spin 99 motor controllers. These controllers are designed for the appropriate power levels, but are intended for use with NiMH or Li based batteries that have low series resistance compared to the fuel cell. As a result, the no-load voltage in our fuel cell system is significantly in excess of the voltage rating of the parts used in these controllers. We disassembled the Spin 99 controllers and replaced the power MOSFETS and capacitors with higher voltage rated parts.

2.3.1.4 Propeller

The propeller determines the relationship between motor speed and load torque, and, therefore, ultimately determines the operating point of the propulsion system. Typically, propeller performance is expressed using dimensionless thrust coefficient C_T and power coefficient C_P. The coefficients are functions of the relative speed of the craft and the prop, or the advance ratio

$$J = \frac{S}{n_p L} \tag{8}$$

where S is the air speed, $n_p = \frac{\omega}{2\pi}$ is the rotational speed of the prop in revolutions per second, and L is the prop diameter [11]. Given C_P at a particular advance ratio, the shaft power required is

$$P = C_P \rho L^5 {n_p}^3 \tag{9}$$

where ρ is the local air density. Setting the propeller power requirement equal to the mechanical power at the shaft, i.e. $\tau\omega = P$, yields the desired relationship between motor speed and torque

$$\tau = C_P \rho L^5 \frac{\omega^2}{(2\pi)^3} \tag{10}$$

Similarly, given C_T , the thrust produced by the propeller is

$$T = C_T \rho L^5 {n_p}^3 \tag{11}$$

The relationship between thrust and air speed is complex, and requires an understanding of the aerodynamic properties of the vehicle and the flight profile. We generally calculate available thrust at a target airspeed. If this number is in excess of the thrust requirement anticipated by the airframe designer, we predict the craft will fly. The relationship between C_T , C_P, and J is captured in the simulation program by second order polynomial functions with coefficients for each propeller. In the laboratory, we tested four APC composite propellers. The specifications for these propellers and manufacturer supplied C_T and C_P functions are listed below. The first number in the propeller specification is the diameter in inches, while the second number is the pitch in inches.

Table 2. Propellers Tested
List of the Propellers used in the Study and their 2nd Order C_T and C_P Polynomials.

Propeller	*Coefficients*
APC 22 x 12	$C_T = -0.039J^2 - 0.055J + 0.062$ $C_P = -0.049J^2 - 0.001J + 0.031$
APC 24 x 12	$C_T = -0.038J^2 - 0.055J + 0.057$ $C_P = -0.045J^2 - 0.005J + 0.028$
APC 26 x 15	$C_T = -0.040J^2 - 0.053J + 0.067$ $C_P = -0.053J^2 - 0.002J + 0.042$
APC 27 x 13	$C_T = -0.037J^2 - 0.055J + 0.054$ $C_P = -0.044J^2 - 0.005J + 0.026$

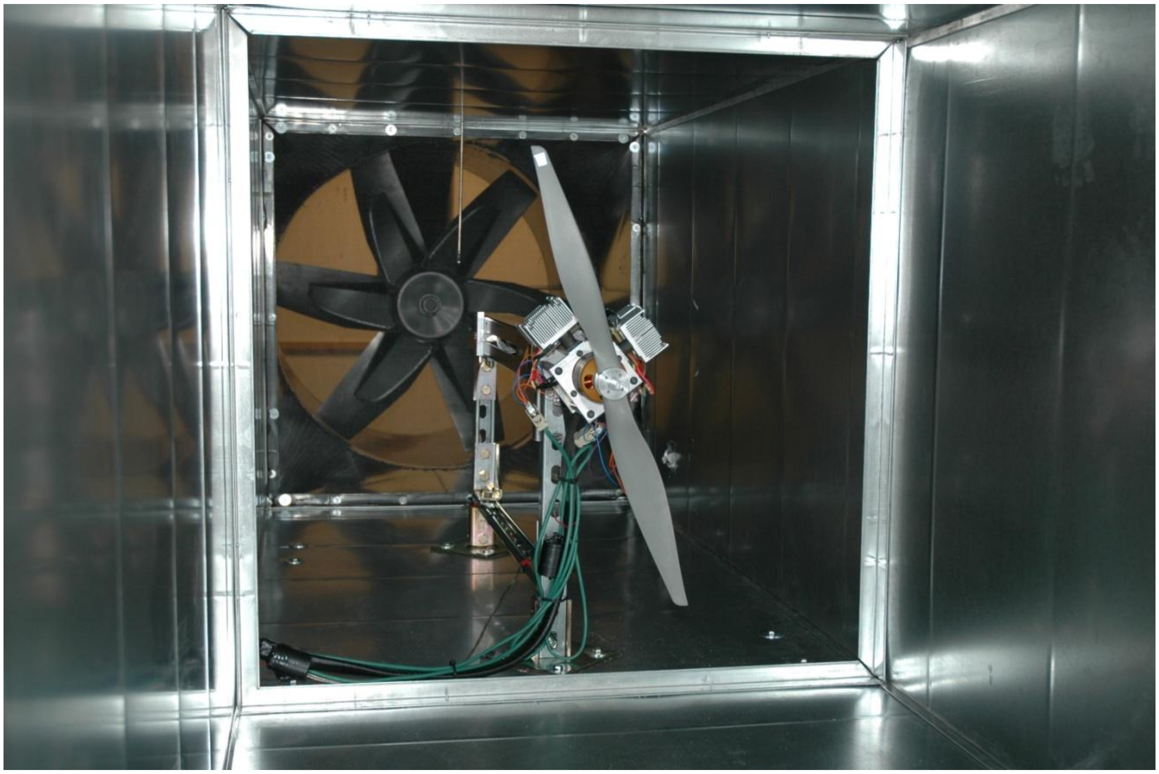

Figure 27. Test Stand.
The Test Stand Used for Testing Motor and Propeller Combinations Installed Inside the Constructed Wind Tunnel

2.3.2 Experimental Setup

An open circuit wind tunnel was constructed for the purpose of testing propulsion systems under flight conditions. The working section of the wind tunnel is 91 cm by 91 cm and 3 m in length. The wind tunnel is excited by a 3.7 kW, 91cm diameter Dayton tub-axial duct fan. As recommended by Mehta and Bradshaw [12], several different combinations of screens and honeycombs were installed in an effort to normalize the air flow through the wind tunnel, as measured by a Kestrel 3500 weather meter. However, these modifications actually created a less uniform flow and were ultimately removed.

A test stand was mounted in the working section of the wind tunnel. The test stand consists of an interchangeable motor mounting plate fixed to a steel rod. The rod is supported at its center of gravity on a pillow block, so that it is free to translate and rotate. The rod is constrained by only a Cooper LXT920 torque/force load cell which provides direct measurement of motor torque and developed thrust. In addition to torque and thrust, we measure atmospheric conditions, air speed, propeller speed, fuel cell current and voltage, and duty cycle on the controller. This allows a full comparison of all simulation variables with lab measurements. The propeller is mounted in a pusher configuration. A mock UAV body can be installed on the test stand to simulate the effect of occluding the propeller with the airframe. Figure 27 shows a picture of the test stand installed inside the wind tunnel.

An experiment is performed by calibrating the resistor to the desired fuel cell output resistance using a precise meter. The resistor cooling system and excitation fan are then turned on. Any instrumentation offsets are then recorded. The power supply simulating the fuel cell is then adjusted to the required open circuit Thevenin equivalent voltage. The duty cycle command is then adjusted until the desired operating point is achieved. All variables are recorded.

2.4 Results & Discussion

2.4.1 Simulation Results and Discussion

With a user-specified controller duty cycle D and airspeed, the combined model equations can be solved with standard techniques to find the system operation point. While this solution is valuable information, it does not provide design insight needed to understand trade-offs in fuel cell output characteristics, control opportunities, or the relative merit of different propeller and motor combinations.

Rather than solving for a single operating point, we find it more useful to solve for a collection of operating points that can be presented in a graphical format. The most intuitive independent variable for this purpose appears to be the fuel cell terminal current, I_c. Numerically, we constrain I_c to a succession of values from a vector, and use the matlab command fsolve() to determine every other variable as a function of current. The outputs are then reflected to the fuel cell terminals where they can be interpreted on one plot in conjunction with the fuel cell response.

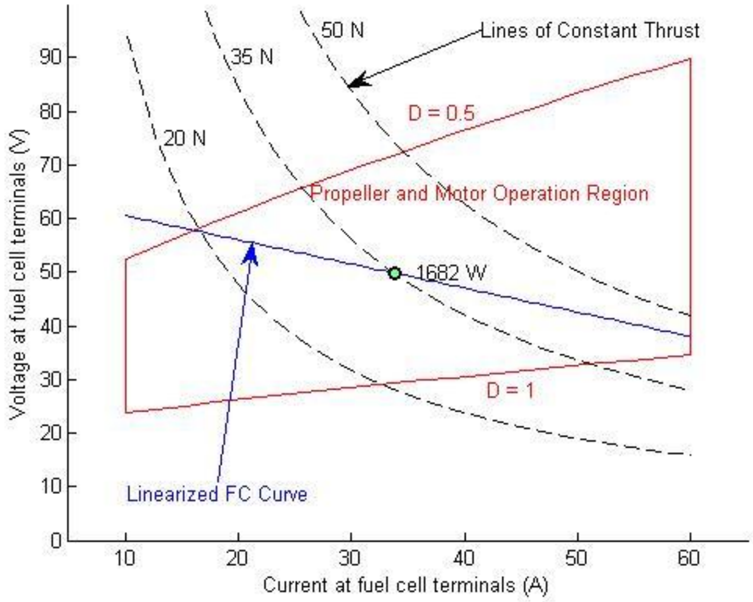

Figure 28. Simulation Results for a Well Designed System. Predicted Performance of the AXI 5345-18 Motor, Jeti Spin 99 Controller, and APC 27 x 13 Propeller. The Simulation was Performed Assuming a cruising Velocity of 30 m/s and Air Density of 1.2 kg/m^3.

Figure 28 shows a sample output. The line labeled "linearized FC curve" is simply a plot of the output characteristic of the fuel cell stack. In this case, we used an open circuit voltage of 65 V and a Thevenin equivalent resistance of 0.45 Ω. The red box, labeled "propeller and motor operation region", represents a family of voltage/current curves for the motor and propeller combination at the specified airspeed. The lower margin of this box shows the relationship between current and voltage for the motor and propeller with duty cycle $D = 1$. The upper margin of the box is the curve corresponding to $D = 0.5$. The operating point of the propulsion system is determined by the intersection of the motor/propeller curve at a specified duty ratio and the fuel cell curve. Thus, the interpretation of the graph is that any point on the fuel cell curve within the box is an achievable operating point at a reasonable steady-state duty ratio between 0.5 and 1.0. To give some interpretation of the achievable operating points in terms of flight performance, we plot contours of a constant thrust on the same plot. These are the dashed lines labeled with thrust values. The operating point indicated by a large point in Figure 5 shows that a thrust of 35 N can be achieved with this propulsion system, corresponding to an electrical output of 1682 W and a duty cycle of about 0.75. This plot shows a relatively good design, where most of the operating range of the fuel cell is mapped to increasing values of thrust by the propulsion system.

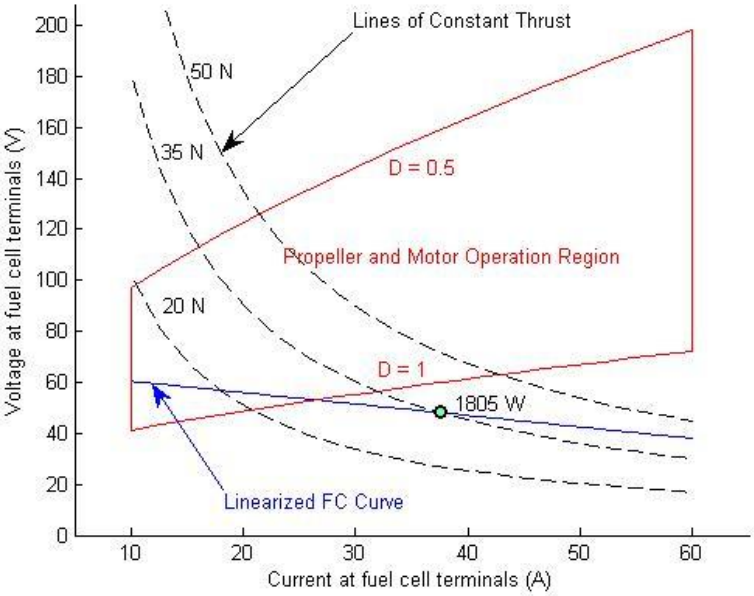

Figure 29. Simulation Results for a Poorly Designed System. Predicted Performance of the AXI 5360 Motor, Jeti Spin 99 Controller, and APC 22 x 12 Propeller. The Smulation was Performed Assuming a Cruising Velocity of 30 m/s and Air Density of 1.2 kg/m^3.

In contrast, Figure 29 shows a poor combination of components for the same fuel cell parameters. In this case, it is not possible to select a duty ratio where the motor and propeller are able to use the power that the fuel cell is capable of delivering. Furthermore, the intersection of the fuel cell curve with the 35 N thrust contour is outside of the propeller curve box, demonstrating that this system is also incapable of producing the thrust achieved by the system in Figure 29. Even if it were possible to command the necessary duty cycle, the simulation shown in Figure 6 would require more power to produce the same thrust.

Graphs of this kind immediately connect the quantities of interest to the fuel cell stack designer, i.e. current and voltage at the stack terminals, to the ability to command thrust, which is of interest to the airframe designer. Furthermore, the graphs lend themselves to understanding how the current/voltage characteristics of a fuel cell might be modified with an auxiliary source, e.g. photovoltaics or battery, and the effect that the new current/voltage characteristic might have on flight performance. As a specific example, the inherently sloping fuel cell curves tend to become parallel to lines of constant thrust at higher currents. Even if the fuel cell is subjected to severe high-current loading, very little additional thrust is possible. On the other hand, an alternate source with a flat current voltage characteristic could be used to temporarily cross several thrust curves and substantially increase the flight envelope.

The appendix contains propeller curve box simulation results for all the propeller and motor combinations overlaid on a linearized fuel cell curve based on the 74-cell, 3 kW PNNL fuel cell stack with parameters V_{oc} = 67.5 V, R_{th} = 300 mΩ, and a proposed operating voltage of V_c = 45.6 V.

2.4.2 Experimental Results and Discussion

Simulations using the model suggested that the best propeller and motor configurations include combinations of the AXI5345-16 and AXI5345-18 motor and APC 24x12 and APC 27x13 propellers. In particular, simulations with these components indicated that a target thrust of 35 N was well within the propeller operation region. Other combinations of components provided lower thrust at higher stack output power.

The components were assembled on the test stand in our wind tunnel and tested at a variety of operating points to verify the simulation results. Figure 30 shows a comparison of measured and predicted thrust and propeller speed respectively, with stack current as the independent variable for the AXI5345-18 and APC 27x13 combination.

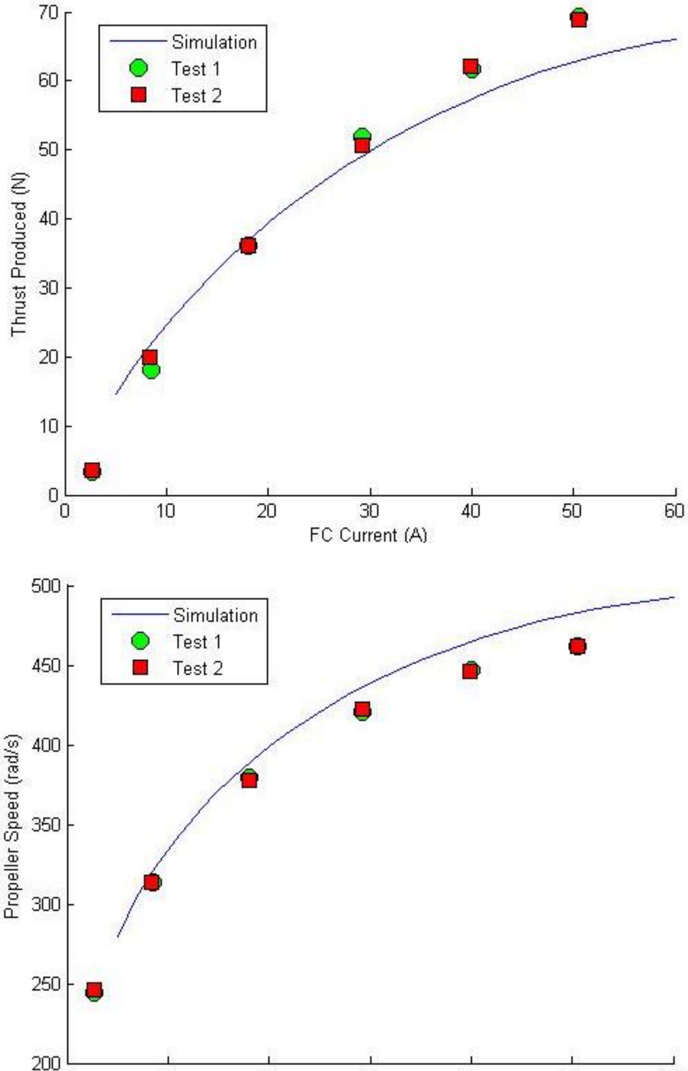

Figure 30. Wind Tunnel Test Results
Predicted Performance and Wind Tunnel Test Results of the AXI5345-18 Motor, Jeti Spin 99 Controller and the APC 27 x 13 Propeller in use with a Linearized Fuel Cell Model Assuming V_{oc} = 65 V and R_{th}=0.45 Ω. For Both Tests, Air Density was Calculated to be Around 1.2 kg/m^3 and Wind Tunnel Velocity Averaged Around 11.6 m/s.

Experimental results generally show good agreement between measured and predicted quantities of the propulsion system model developed in this paper. An exception is that the measured thrust in the wind tunnel exceeds the model result, and the measured propeller speed is slightly lower than the model prediction. These deviations are likely due to a combination of factors, including modeling errors that tend to increase system efficiency in the simulations, partial occlusion of the propeller by the test stand, and flow characteristics in the wind tunnel. The ratio of propeller swept area to wind tunnel cross section area is between 29% and 45% for our propeller choices, so it is likely that the wind tunnel blockage effects described in Fitzgerald and Corrigan [13, 14] affect the measurements to some degree. Finally, we need to extrapolate from the velocities achieved in our wind tunnel, which are roughly 12 m/s, to flight speeds. Despite these limitations, the agreement of experimental and predicted results provides some confidence that a given fuel cell / electric propulsion system design will fly successfully.

2.5 Conclusions

This report presented a physically-based steady-state solution model for design and optimization of a fuel cell powered UAV propulsion system. The individual components and their models were described in detail in the methods, assumptions, and procedures section. The simulation program described in the first half of the results and discussion section combines these models to provide a graphical procedure allowing easy assessment of the design trade offs for the components of the propulsion system including the fuel cell, motor, controller, and propeller. In the second half of the results and discussion section, results from wind tunnel tests of propulsion system components were given. These results generally show good agreement with the predicted performance given by the simulation program. From this agreement, we have confidence that the models comprising the simulation program are sound and that the program is a useful tool for selecting good combinations of propulsion system components.

Additionally, we have found that expressing the simulation results graphically is extremely useful in coordinating the efforts of multiple groups involved in building a fuel cell / electric propulsion system. Stack designers can immediately appreciate the implications of increasing the height of the stack or changing cell thickness, simply by sketching a new fuel cell curve on the plot. The effect of power source hybridization or alternate power electronic topologies can be displayed on the same graph by adding the associated curves to the plot. Finally, the implications of design changes in the fuel cell / electric propulsion are immediately apparent to the air frame design team.

2.6 Recommendations

In consideration of the research conducted by the authors to date regarding fuel cell powered UAVs, further attention should be given to verifying the component models, particularly the propeller models, through wind tunnel tests. At the time of this report, not all combinations of system components have been thoroughly tested. Further, a better understanding of the effects of the wind tunnel blockage described in Fitzgerald and Corrigan [13, 14] is needed for the wind tunnel tests to give stronger assurance of the validity of the propeller model used in the simulation program. Alternatively, system tests in a much larger wind tunnel where wind tunnel blockage would be minimized would also add confidence to the simulation programs accuracy.

Looking beyond the focus of this report, future research should consider the implications of adding an auxiliary power source for increased range of propulsion performance and protection of the fuel cell from transient load requirements. Also, dynamic models for the system components should be included in future versions of the simulation program.

3.0 REFERENCES

[1] U. C. Ofoma, C. C. Wu, “Design of a Fuel Cell Powered UAV for Environmental Research,” *AIAA 3rd Unmanned Unlimited Technical Conference, Workshop and Exhibit*, Chicago, Illinois, Sep. 20-23, 2004.

[2] D. S. Soban, E. Upton, “Design of a UAV to Optimize Use of Fuel Cell Propulsion Technology,” *Infotech@aerospace*, Arlington, Virginia, Sep. 26-29, 2005.

[3] B. A. Moffitt, T. H. Bradley, D. E.Parekh, and D. Mavris, “Design and Performance Validation of a Fuel Cell Unmanned aerial Vehicle,” *44th AIAA Aerospace Sciences Meeting and Exhibit*, Reno, Nevada, Jan. 9-12, 2006. Jan. 1997.

[4] S. Pasricha and S. R. Shaw, “A Dynamic PEM Fuelcell Model”, *IEEE Transactions on Energy Conversion*, vol. 21,pp. 484–490, June 2006.

[5] S. Pasricha, M. Keppler, S. R. Shaw and M.H. Nehrir,“Comparison and Identification of Static Electrical Terminal Fuel Cell Models”, *IEEE Transactions on Energy Conversion*, vol. 22,pp. 746–754, September 2007.

[6] “Fuel Cell Handbook Seventh Edition”, U.S. Department of Energy.

[7] S. Ogasawara, and H. Akagi, “An Approach to Position Sensorless Drive for Brushless dcMotors,” *IEEE Transactions on Industry Applications*, vol. 27, pp. 928–933, Sept.-Oct. 1991.

[8] H. A. Toliyat, and G. B. Kliman, *Handbook of Electric Motors*. Taylor & Francis Group, 2004.

[9] C. G. Kim, J. H. Lee, H. W. Kim and M. J. Youn, “Study on Maximum Torque Generation For Sensorless Controlled Brushless DC Motor With Trapezoidal Back EMF,” *Electric Power Applications, IEEE Proceedings*, vol. 152, pp. 277–291, March 2005.

[10] P. Yedamale, *Brushless DC (BLDC) Motor Fundamentals*, Microchip Technologies, 2003.

[11] B. W. McCormick, *Aerodynamics, Aeronautics, and Flight Mechanics*. John Wiley & Sons, 1979.

[12] R. D. Mehta, and P. Bradshaw, “Design Rules for Small Low Speed Wind Tunnels,” *Aeronautical Journal*, pp. 443–4491, November 1979.

[13] R. E. Fitzgerald, *Wind Tunnel Blockage Corrections for Propellers*. Masters Thesis, University of Maryland, Department of Aerospace Engineering, 2007.

[14] E. K. Corrigan IV, *Survey of Small Unmanned Aerial Vehicle Electric Propulsion System*. Masters Thesis, University of Dayton, Department of Aerospace Engineering, December 2007.

4.0 LIST OF ACRONYMS, ABBREVIATIONS, AND SYMBOLS

Acronyms & Abbreviations

UAV – Unmanned Aerial Vehicle
PEM – Proton Exchange Membrane
FC – Fuel Cell
SOFC – Solid Oxide Fuel Cell
SEM – Scanning Electron Micrograph
BLDC – Brushless Direct Current
NiMH – Nickel Metal Hydride
Li – Lithium

Fuel Cell Symbols

I_C – fuel cell current (A)
V_C – fuel cell voltage (V)
R_{th} – fuel cell model Thevenin equivalent resistance (Ω)

Motor & Motor Controller Electric Symbols

I_m – effective motor current (A)
V_m – effective motor voltage (V)
R_m – per phase winding resistance (Ω)
D – duty cycle
τ_e – torque of electric origin (N-m)
I_0 – no load current (A)
V_0 – no load voltage (V)
β – motor drag coefficient (??)

Motor & Motor Controller Mechanical Symbols

τ – motor mechanical torque (N-m)
ω – motor speed (rad/s)
K – motor speed constant (V-s/rad)
P – shaft power (W)

Propeller Symbols

S – air craft velocity (m/s)
n_p – propeller speed (rev/s)
L – propeller diameter (m)
J – advance ratio
C_P – coefficient of power
C_T – coefficient of thrust
ρ - air density (kg/m^3)
T - produced thrust (N)

APPENDIX A

High Performance, High Power Density Solid Oxide Fuel Cells

Load Control

Complete Collection of Simulation Results

The complete collection of simulation results for all combinations of AXI Motors and APC propellers listed in Table 1 and Table 2 (in the body of the report), respectively are compiled in this section. The propeller curve box described in the simulation results section for each combination is over laid on the linearized fuel cell model for the 74-cell 3 kW PNNL SOFC stack with parameters V_{oc} = 67.5 V, R_{th} = 300 mΩ and a proposed operating voltage of V_c = 45.6 V. In all cases, the air density was assumed to be 1.2 kg/m^3, and the air craft velocity was assumed to be 31.3 m/s. The operation point is dictated by the blue dot and next to it the resulting predicted thrust is listed.

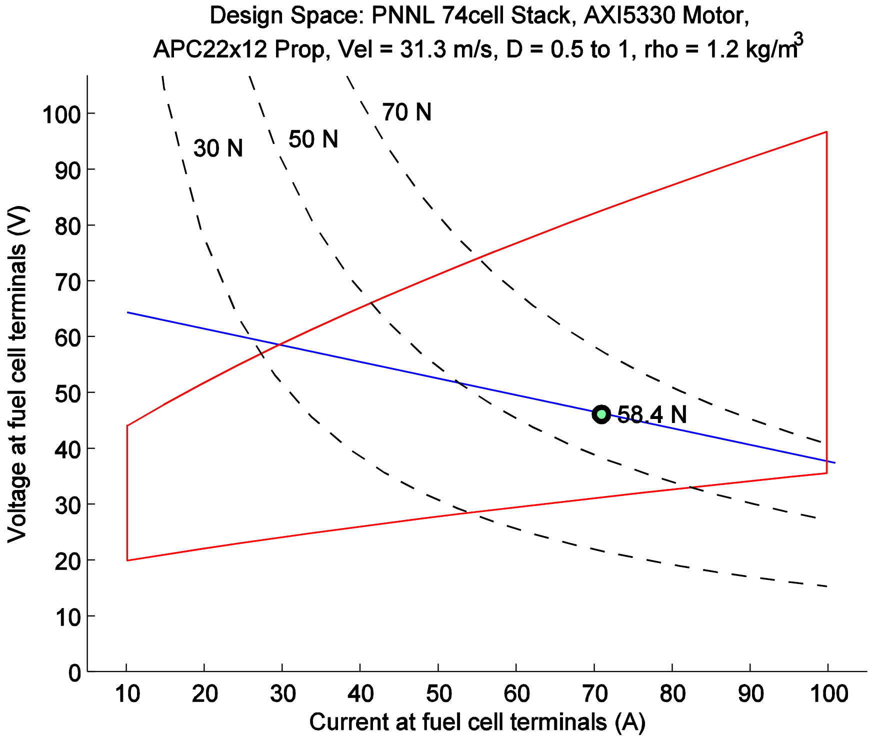

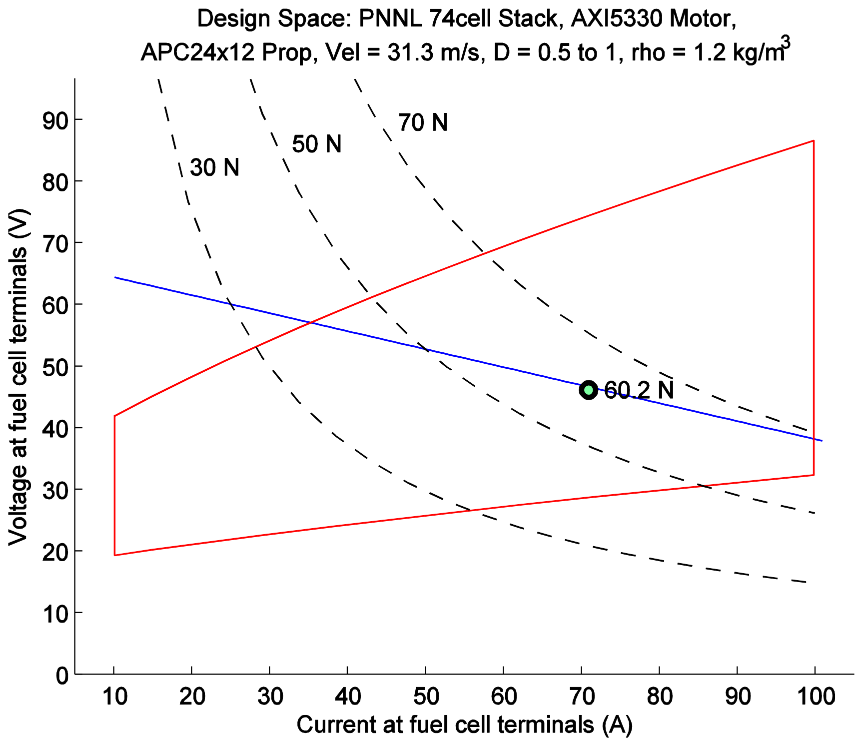
Design Space: PNNL 74cell Stack, AXI5330 Motor,
APC24x12 Prop, Vel = 31.3 m/s, D = 0.5 to 1, rho = 1.2 kg/m3
Voltage at fuel cell terminals (V)
Current at fuel cell terminals (A)
0
10
20
30
40
50
60
70
80
90
100
30 N
50 N
70 N
60.2 N

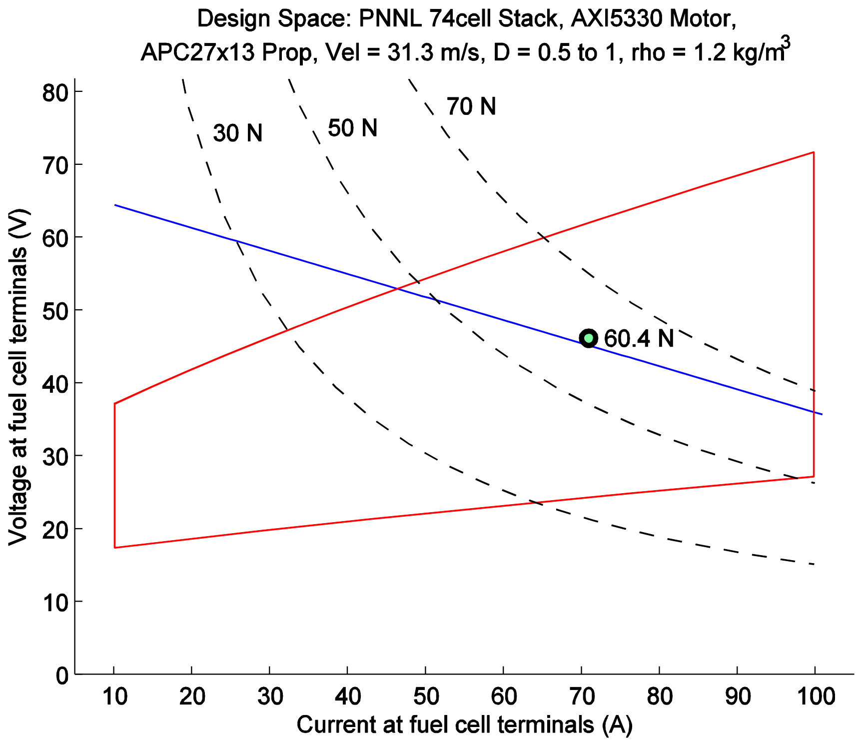
Design Space: PNNL 74cell Stack, AXI5330 Motor,
APC27x13 Prop, Vel = 31.3 m/s, D = 0.5 to 1, rho = 1.2 kg/m^3
Voltage at fuel cell terminals (V)
Current at fuel cell terminals (A)
0
10
20
30
40
50
60
70
80
10
20
30
40
50
60
70
80
90
100
30 N
50 N
70 N
60.4 N

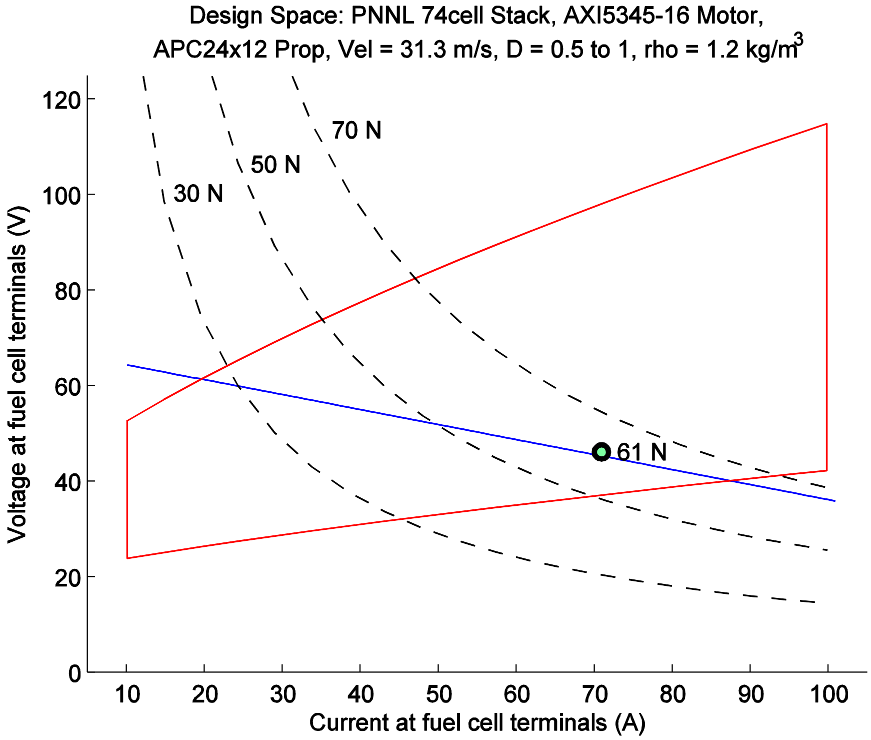
Design Space: PNNL 74cell Stack, AXI5345-16 Motor,
APC24x12 Prop, Vel = 31.3 m/s, D = 0.5 to 1, rho = 1.2 kg/m^3
Voltage at fuel cell terminals (V)
Current at fuel cell terminals (A)
0
20
40
60
80
100
120
10
20
30
40
50
60
70
80
90
100
30 N
50 N
70 N
61 N

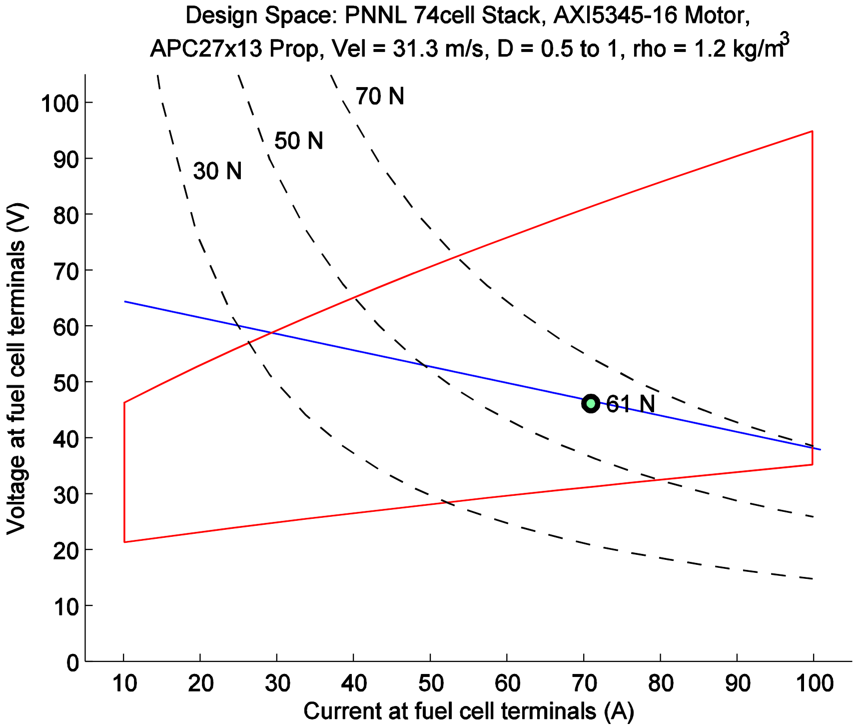

Design Space: PNNL 74cell Stack, AXI5345-16 Motor,
APC27x13 Prop, Vel = 31.3 m/s, D = 0.5 to 1, rho = 1.2 kg/m^3
70 N
50 N
30 N
61 N
Voltage at fuel cell terminals (V)
0
10
20
30
40
50
60
70
80
90
100
10
20
30
40
50
60
70
80
90
100
Current at fuel cell terminals (A)

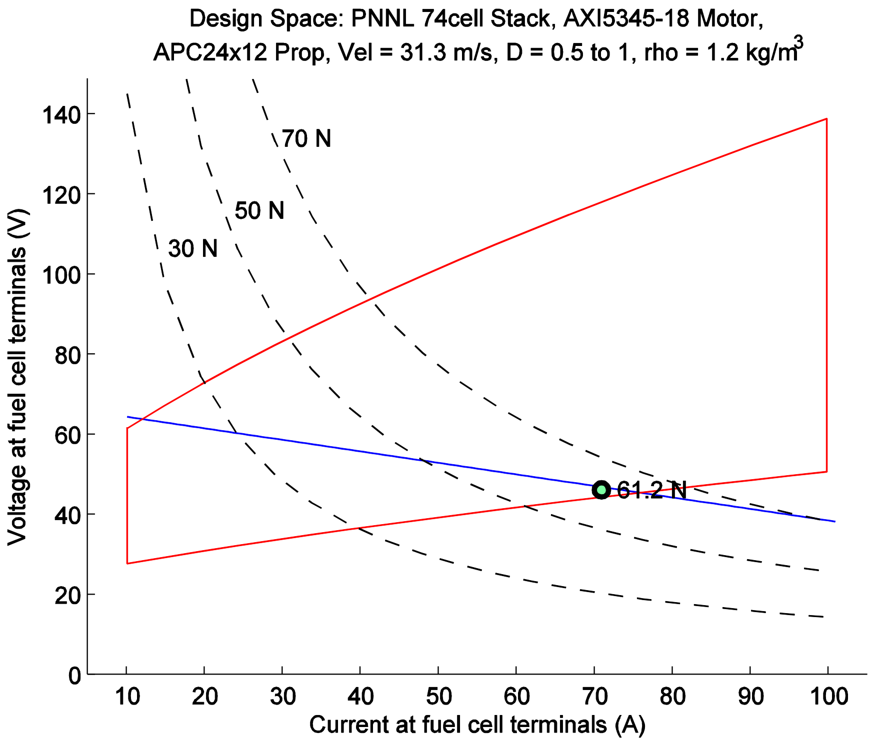
Design Space: PNNL 74cell Stack, AXI5345-18 Motor,
APC24x12 Prop, Vel = 31.3 m/s, D = 0.5 to 1, rho = 1.2 kg/m^3
Voltage at fuel cell terminals (V)
0
20
40
60
80
100
120
140
Current at fuel cell terminals (A)
10
20
30
40
50
60
70
80
90
100
30 N
50 N
70 N
61.2 N

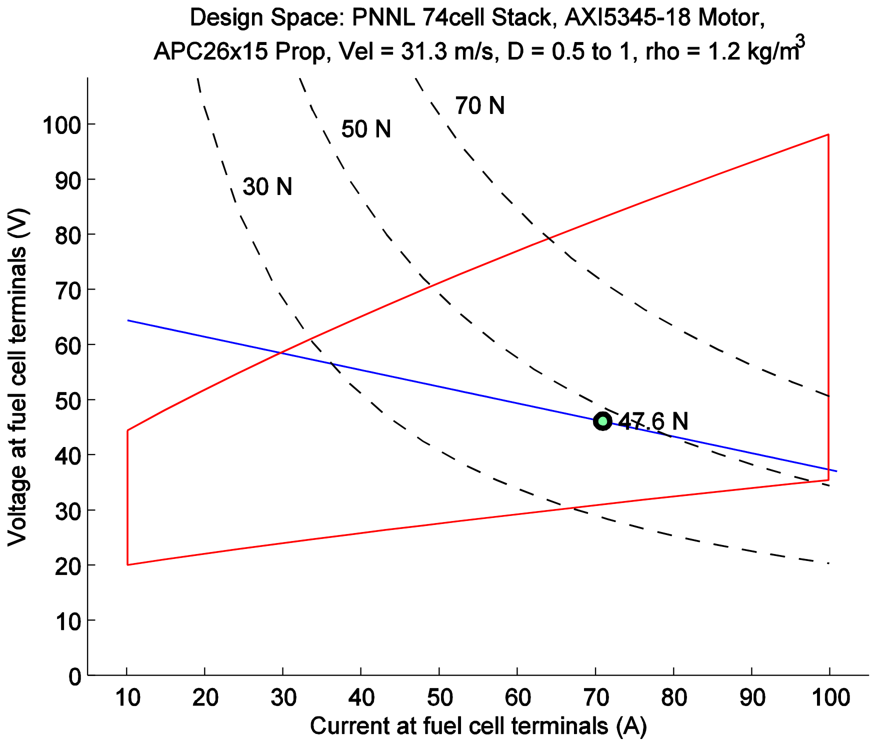
Design Space: PNNL 74cell Stack, AXI5345-18 Motor,
APC26x15 Prop, Vel = 31.3 m/s, D = 0.5 to 1, rho = 1.2 kg/m3
70 N
50 N
30 N
47.6 N
Voltage at fuel cell terminals (V)
0
10
20
30
40
50
60
70
80
90
100
10
20
30
40
50
60
70
80
90
100
Current at fuel cell terminals (A)

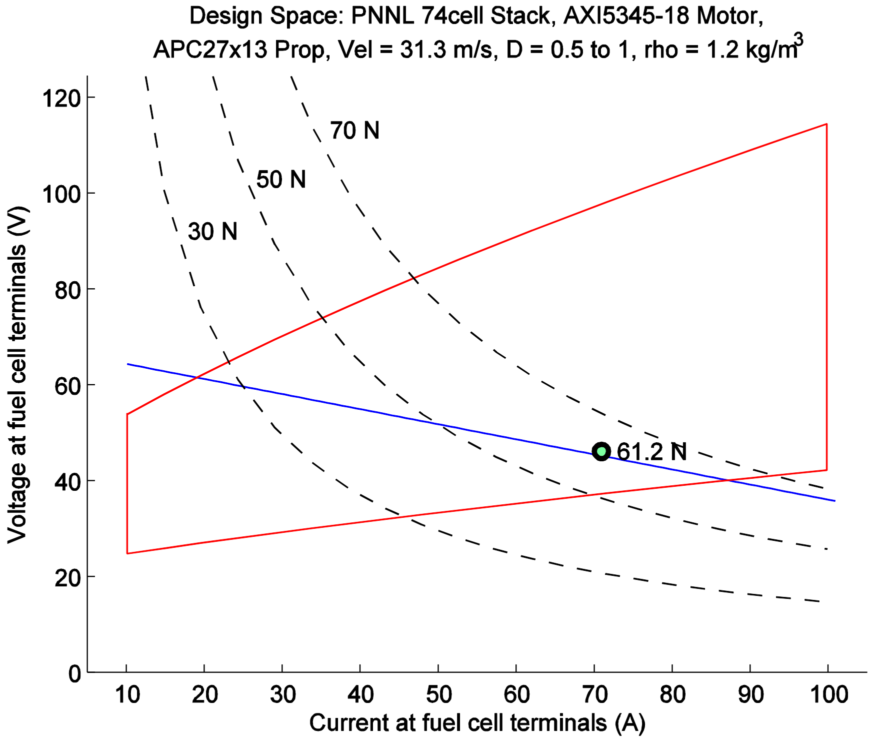
Design Space: PNNL 74cell Stack, AXI5345-18 Motor,
APC27x13 Prop, Vel = 31.3 m/s, D = 0.5 to 1, rho = 1.2 kg/m3
70 N
50 N
30 N
61.2 N
Voltage at fuel cell terminals (V)
0
20
40
60
80
100
120
10
20
30
40
50
60
70
80
90
100
Current at fuel cell terminals (A)

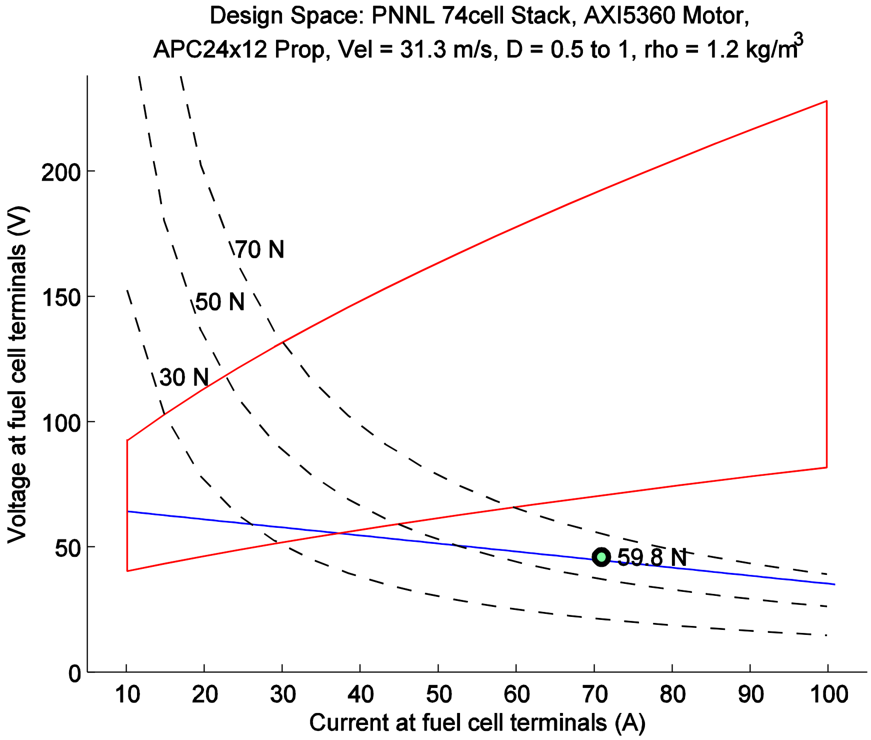
Design Space: PNNL 74cell Stack, AXI5360 Motor,
APC24x12 Prop, Vel = 31.3 m/s, D = 0.5 to 1, rho = 1.2 kg/m^3
Voltage at fuel cell terminals (V)
0
50
100
150
200
Current at fuel cell terminals (A)
10
20
30
40
50
60
70
80
90
100
70 N
50 N
30 N
59.8 N

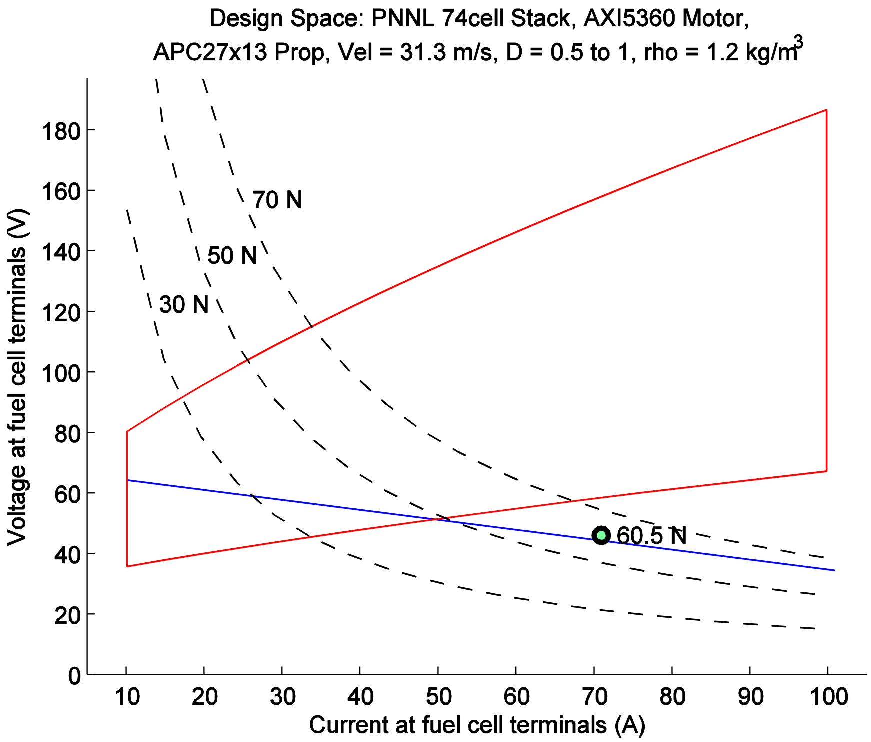
Design Space: PNNL 74cell Stack, AXI5360 Motor,
APC27x13 Prop, Vel = 31.3 m/s, D = 0.5 to 1, rho = 1.2 kg/m^3
Voltage at fuel cell terminals (V)
Current at fuel cell terminals (A)
0
20
40
60
80
100
120
140
160
180
10
20
30
40
50
60
70
80
90
100
70 N
50 N
30 N
60.5 N